UC Irvine
UC Irvine Electronic Theses and Dissertations

Title
Hybrid Microfabrication Techniques for Microelectrode Arrays

Permalink
https://escholarship.org/uc/item/9wj0h841

Author
Chang, Spencer Chen Wen

Publication Date
2014

Peer reviewed|Thesis/dissertation

eScholarship.org Powered by the California Digital Library
University of California

UNIVERSITY OF CALIFORNIA,
IRVINE

Hybrid Microfabrication Techniques for Microelectrode Arrays

THESIS

submitted in partial satisfaction of the requirements
for the degree of

MASTER OF SCIENCE

in Biomedical Engineering

by

Spencer Chen Wen Chang

Thesis Committee:
Assistant Professor Mark Bachman, Chair
Professor John C. Middlebrooks
Professor Guann-Pyng Li

2014

© 2014 Spencer Chen Wen Chang

TABLE OF CONTENTS

LIST OF FIGURES iii
ACKNOWLEDGEMENTS iv
ABSTRACT OF THE THESIS v
CHAPTER 1: INTRODUCTION 1
1.1 Neural Stimulation 1
1.2 Microelectrode Arrays 3
1.3 Hybrid Microfabrication 6
1.4 Project Goals 8
CHAPTER 2: HYBRID MICROWIRE MICROELECTRODE ARRAY 10
2.1 Introduction: Microelectrode Arrays 10
2.2 Microfabrication of Shank Microelectrode Arrays 12
2.3 Electrode Characterization 20
2.4 Microelectrode Array Configurations 24
2.5 Increasing MEA Surface Area 26
CHAPTER 3: OPTOELECTRODE OPTICAL ELEMENTS 35
3.1 Introduction: Optogenetics and the Optoelectrode 35
3.2 Optical Fiber Tapering 37
3.3 Selective Metallization on Tapered Fibers 41
3.4 Fiber Truncation 44
3.5 Optical Focusing and Scattering 49
CHAPTER 4: FLEXIBLE STIMULATING MICROELECTRODE ARRAY 58
4.1 Introduction 58
4.2 Microfabrication of Flexible Microelectrode Arrays 59
4.3 Future Directions 66
CHAPTER 5: CONCLUSION 69
BIBLIOGRAPHY 71

LIST OF FIGURES

Figure 2.1 Microelectrode Array Overview 11
Figure 2.2 SEM of PMMA Micromolds 14
Figure 2.3 Diagram of Micromold Milling and Drilling Operations 15
Figure 2.4 Diagram of Microwire Threading and Thermal Mechanical Bond Processes 16
Figure 2.5 Diagram of Epoxy Casting in Micromold 17
Figure 2.6 Diagram of Wire Trimming and Tip Forming 18
Figure 2.7 Iridium Oxide Deposition on Exposed Wire Ends 19
Figure 2.8 Average Impedance for As-cut, Conditioned, and IrOx Plated Electrode Sites 21
Figure 2.9 SEM of As-cut, Conditioned, and IrOx plated sites 22
Figure 2.10 Cyclic Voltammogram of IrOx Plated Electrode Sites 23
Figure 2.11 Three-Sided MEA 25
Figure 2.12 Preliminary 3D Lithography Stencil and Resulting Structure 29
Figure 2.13 Machined 3D Lithography Stencil 30
Figure 2.14 3D Patterned Optical Fibers 32
Figure 2.15 Evaporated Metal Bands on Electrode Phantoms 33
Figure 3.1 Diagram of Optical Fiber Structure 36
Figure 3.2 Comparison of Optical Fiber Tapering Methods 38
Figure 3.3 Self Terminating Fiber Etching Technique 39
Figure 3.4 Comparison of Stripped Optical Fibers 40
Figure 3.5 Tapered Fibers Produced with Various Cone Angles 41
Figure 3.6 Tapered Fibers Coated with Silvering Solution 43
Figure 3.7 Fiber Truncation Process 44
Figure 3.8 Tapered Optical Fiber Encapsulated in Sacrificial PMMA Carrier 45
Figure 3.9 Optical Fiber Carrier 47
Figure 3.10 Alignment Jig for Fiber Truncation 47
Figure 3.11 Tapered and Truncated 25 μm Optical Fibers 48
Figure 3.12 Lithographically Formed Microlenses on 25 μm Diameter Optical Fibers 51
Figure 3.13 Through-fiber Exposure of Positive Photoresist on Tapered Fiber 52
Figure 3.14 Cleaved and Broken 25 μm Optical Fibers with Negative Photoresist Structures 53
Figure 3.15 Optical Fibers with Fused Glass Microlenses 54
Figure 3.16 Diagram of Microlens Pre-form Fabrication Process 55
Figure 3.17 Composite Microlenses Formed with EPO-TEK 301 and 5 μm Borosilicate Glass Spheres 57
Figure 4.1 Flexible Polymer MEA Overview 59
Figure 4.2 Photomasks Used in Polymer MEA Fabrication 60
Figure 4.3 Fabrication Process for Polymer MEA 62
Figure 4.4 SEM of Polymer MEAs 63
Figure 4.5 Polymer MEA 66

ACKNOWLEDGEMENTS

I would like to express my appreciation to my committee for their support and guidance: Mark Bachman, my committee chair; John Middlebrooks; and G.P. Li. I cannot express enough thanks for the opportunities provided by my committe.

I would like to thank the past and present members of the MIDAS Lab, especially Mark Merlo for his mentorship, Lily Wu for her support, and Jonas Tsai for his friendship.

Finally, I would like to thank my best friend and partner Jenny Hsieh for her supportiveness and patience. Without your help, this thesis would not have been possible.

ABSTRACT OF THE THESIS

Hybrid Manufacturing Techniques for Microelectrode Arrays

By

Spencer Chen Wen Chang

Master of Science in Biomedical Engineering

University of California, Irvine, 2014

Professor Mark Bachman, Chair

Micro technology has become central to many applications of modern biomedical engineering. As scientists seek to investigate biological systems at the micro and nano level, there has been an increased need for manufacturing techniques capable of producing complex microscale components. Currently, biomedical engineers utilize microfabrication techniques based on semiconductor manufacturing to fabricate microdevices. While these techniques offer microscale resolution, high reproducibility, and batch fabrication, they suffer from narrow material selection, poor integration, and offer limited geometrical complexity. Hybrid microfabrication addresses these limitations by combining modern manufacturing techniques to enable highly integrated devices with complex three-dimensional topologies. In the present study, microelectrode arrays and components were produced using hybrid microfabrication techniques in order to explore the ability to fabricate complex integrated microdevices from a wide range of materials using modern manufacturing techniques. 32-channel recording electrodes were produced using precision tool-based micromachining, microwire assembly, molding, sacrificial release, rotational lithography, and electrodeposition. Optogenetic electrodes were fabricated using selective etching, through-fiber photolithography,

micromolding, embossing, and glass sintering. Finally, planar lithographic techniques were used to create flexible thin-film electrodes. Through a combination of modern manufacturing techniques it was shown that complex microstructures could be produced from a wide range of materials with improved integration.

CHAPTER 1: INTRODUCTION

1.1 Neural Stimulation

Action potentials, created by the rise and fall of the electrical membrane potential of a cell, are the basis of neuronal communication between cells of the central and peripheral nervous system. Microelectrode arrays (MEAs) are valuable research tools that enable the stimulation and recording of neural activity by electrically depolarizing the membrane of excitable cells, or measuring the extracellular potential created by the action potential firing of a single neuron. Beyond the research environment, MEAs chronically interfaced with central and peripheral nervous system serve as the basis for neural prostheses and therapies involving neural stimulation and recording. Applications of recording and stimulating electrodes include upper and lower limb prostheses for stroke and spinal cord injury, cochlear and brainstem auditory prostheses, and deep brain and vagus nerve stimulation treatments for intractable epilepsy, essential tremor, and Parkinson disease [1]–[4]. The varied applications of MEAs have led to the development of electrodes with diverse materials, structures, topologies, and electrical properties.

Stimulating electrodes initiate a functional response in tissue by depolarizing the membranes of excitable cells. A stimulating depolarization occurs when an ionic flow that surpasses a current threshold is generated between two electrodes in the vicinity of excitable cells [5]. The response of the stimulation is affected by the distance of the electrodes to the tissue being stimulated, and electrodes placed on the surface of neural tissue require higher threshold current levels to evoke a functional response than those implanted within neural tissue [6]. Neural stimulation methods involve injecting biphasic current pulses with charge-balanced

anodal and cathodal current amplitudes and pulse durations in order to avoid tissue damage and degradation of the electrode [7]. Stimulating pulses are characterized by the total charge and charge density delivered in the leading phase, current density, the pulse width of each phase, and frequency of the stimulating pulse, where the geometrical surface area (GSA) of the electrode sites is used to determine the charge and current densities [5]. The charge and current densities to allow charge injection by reversible electrochemical processes. Surpassing the limits for safe stimulation can result in electrolysis of water and the release of hydrogen, oxidation of the metal electrode, and dissolution of metal ions into the surrounding tissue [8]. Maintaining safe reversible charge injection is a core requirement for all stimulating electrodes.

In general, stimulation electrodes are categorized as either macroelectrodes or microelectrodes. Macroelectrodes have GSA greater than 100,000 μm^2 and are often oriented on the surface of the target tissue. The large surface areas of macroelectrodes allow for high charge injection with low charge density. Microelectrodes on the other hand are classified as those having GSA smaller than 10,000 μm^2 and typically penetrate the tissue of interest [5]. Macroelectrodes are less prone to electrochemical corrosion due to low charge densities, but high charge levels can induce tissue damage when subjected to chronic stimulation. The high charge densities encountered in microelectrode stimulation contribute to higher levels of stimulation-induced tissue damage and electrode degradation. However, microelectrodes are able to increase selectivity by stimulating smaller volumes of tissue, and multiple microelectrodes in conjunction can provide higher spatial resolution of functional responses.

Electrodes that measure neural activity by monitoring the change in extracellular potential over time are known as recording electrodes. Depolarization and repolarization across cell membranes caused by the firing of action potentials can be detected in the extracellular vicinity

of the cells via changes in the electric potential across two electrodes. Neural signal noise provides a significant challenge while recording single-unit firing of action potentials from individual cells. The major sources of signal noise during neural recording are undifferentiated background action potentials and the impedance of the recording electrode. For chronic recording of action potentials, signal-to-noise greater than 5:1 are desirable, and several techniques are employed to improve signal-to-noise ratio, including using multiple electrodes for signal triangulation, minimizing of the distance between electrode and signal source, and reducing electrode impedance through material selection and topology [9][10]. Unlike stimulating electrodes, the current flow across the electrode-tissue interface is minimal during recording and electrochemical degradation and tissue damage are infrequently encountered with recording electrodes. The primary design requirement for recording electrodes is low impedance for improved signal-to-noise ratio during recording.

1.2 Microelectrode Arrays

Current MEA styles generally fall into one of two categories: microwire electrode arrays assembled from groups of electrically insulated wires, and lithographically defined planar MEAs. Microwire electrodes, representing one of the most successful types of chronically implanted recording electrodes, are created from insulated tungsten, stainless steel, gold, or platinum/iridium wires with diameter ranging from 25 – 100 μm [11]. Each wire represents a single electrode site, and the distal ends of the insulated microwires are sharpened or otherwise exposed to enable the stimulation or recording of neuronal signals only in the vicinity of each tip. Multi-dimensional microwire arrays are fabricated by stacking rows of microwires that have been pre-assembled in alignment fixtures. Multiple wires of equal length can be arranged to

create two-dimensional arrays with all electrode sites in a single plane, or wires with varying lengths can be used to create three-dimensional microwire arrays [12]. The microwire MEA fabrication process enables complex configurations of microwires in the three-dimensional space, and allows precise spatial control in neural recordings [13]. This fabrication method does not rely on specific interactions between materials and can therefore be easily adapted to a wide selection of materials. In addition, the fixture based assembly methods provide for seamless integration of the electrode with its interconnecting cables, packaging, and interfacing connectors. However, microwire electrode fabrication is limited in that it does not scale well for mass-production/batch fabrication, and does not offer multiple electrodes on each shank.

MEAs created using photolithography frequently consist of a thin electrode shank with multiple electrode sites along its length. Lithographically defined MEAs are typically formed from silicon and silicon dioxide and silicon nitride dielectrics by bulk or surface micromachining processes, or frequently a combination of both [11], [14]–[16]. Bulk micromachining involves selective etching of a thick substrate whereas surface micromachining describes the deposition and etching of structural layers. By using microelectromechanical systems (MEMS) fabrication processes and integrated circuit technology, high quantities of electrodes with GSA ranging from tens to thousands of micrometers-squared can be batch manufactured with sub-micrometer precision [17].

However, lithographically fabricated electrodes are not without their limitations. While lithographic fabrication methods offer batch fabrication of MEAs, reproducibility, small size, and are capable of integrating on-chip electronics and fluidics, the increasing complexity of the devices are reflected in their intricate multi-step fabrication that can require tens of photolithographic masks, with each mask involving multiple step processes and must be

sequentially aligned with sub-micrometer precision [17], [18]. Photolithography is an inherently planar process and the direct creation of complex three-dimensional structures is often not possible. Lithographic processes typically require planar substrates and the topologies of the structures defined by sequential stacking of two-dimensional layers. Three-dimensional arrays can be assembled by stacking multiple sets of planar electrode shanks, but the added processing increases manufacturing complexity and decreases device yield [19]. Complex three dimensional structures are difficult or impossible to fabricate using photolithography exclusively without the use of complicated optical units and substrate stages or specialized techniques such as anisotropic etching or diffusion-mediated direct writing [20]. While planar electrodes benefit from batch fabrication, both monolithic electrodes and micro-assembled MEAs require individual packaging to construct functional devices.

Lithographic fabrication processes suffer from limited materials selection. Most current processes used to manufacture planar electrodes are adapted from silicon based integrated circuit and microelectronic technology. Single-crystal silicon has been a primary substrate used in the microelectronics industry because of its excellent electrical properties and unique high precision machinability [21]. Polymer substrates have also been utilized in planar electrode fabrication [22]. Many of the processes involved in planar electrode fabrication depend on specific chemical interactions with the substrate and modification or substitution of materials is rarely possible. In addition, integration of many types of device is not possible because of incompatibility with the lithographic processes necessary to planar electrode fabrication. While great success has been achieved by recording and stimulating with silicon electrodes, inherent limitations have hindered the integration of new materials, processes, and devices with silicon MEAs.

1.3 Hybrid Microfabrication

Microfabrication describes fabrication techniques that are capable of producing components with features in the range of several to hundreds of micrometers with micrometer precision. Microfabricated components are becoming staples for a growing list of fields including optics, electronics, medicine, biotechnology, and communications to name a few [23]. The drive towards miniaturization technology in manufacturing has led to significant progress in the development of diverse microfabrication techniques, which include lithography, film deposition, etching, polishing and grinding, electroplating, stamping, embossing, micromolding, and micromachining through micro cutting, drilling, and milling. The driving force behind photolithographic technology is the microelectronics industry, whose demand for smaller part sizes and higher capacity has led to highly developed silicon-based manufacturing technologies with sub-micrometer resolution, batch manufacturing, and high reproducibility. MEMS device technology incorporating lithography, physical and chemical deposition, and wet and dry etching has led to sophistication in the ability to create parts from stacks of two dimensional layers with micro and nano sized features. Ultra-precision grinding and polishing have been instrumental in the preparation of silicon wafers for the microelectronics and MEMS industry as well as micro optical devices where surfaces in the order of 10 nm are required [24]. Forming of materials through the use of stamping, embossing, and micromolding is routinely achieved with metals, polymers, and ceramics, and can result in components with features in the sub-micrometer range and aspect ratios of 10-15, but is largely dependent on the quality of the stamp or mold [25], [26]. Tool-based micromachining is capable of fabricating complex three-dimensional structures from metal, polymer, ceramic, and glass substrates with micrometer precision and aspect ratios greater than 50:1 [27]. Many of these processes have become staples in the manufacturing

industry and as a result have seen steady improvements in terms of reliability, reproducibility, and throughput.

The constant demand for reduced weight and dimensions, higher surface quality and part accuracy continues to push the limits of microfabrication processes beyond their current capabilities [28]. In order to meet these demands, new design principles and methodologies must be established to allow for greater integration of manufacturing processes. Traditionally, microfabrication is performed on precision machine tools having conventional dimensions, but as feature size decreases, machine resolution and precision are increasingly susceptible to dimensional changes from heat deformation, vibration, and have relatively high rates of material consumption [29]. Alternatively, microfactory systems have been proposed in which machine tools are miniaturized to address the limitations of larger machines and create economic benefits in terms of energy reduction, floor space reductions, and structural cost savings [30]. Scaling down existing processes plays a critical role in the development of current microfabrication techniques, but the development of new strategies for integrating processes such as handling, fabrication, assembly, packaging, quality assurance, and metrology are necessary for the future of microfabrication [29].

While the exact development pathway for the microfabrication of smaller, more complex microdevices is uncertain, it is evident that integration of diverse processes through hybrid microfabrication techniques is necessary to create fully integrated microdevices. Hybrid microfabrication involves combining microfabrication techniques to enable the fabrication of unique structures with a large material selection. Most microfabrication processes have limitations which make any individual process unsuitable for fabricating entire devices. For example, lithography lacks the ability to create complex three-dimensional structures and has

limited material selection and tool based micromachining struggles with handling of microscale components. By combining components from diverse microfabrication techniques, new processes pathways that integrate the handling, fabrication, assembly, packaging, and measurement of microdevices can be realized. Hybrid techniques such as the sacrificial release of micromachined parts by selective etching, die separation of silicon devices with wafer dicing saws, and overmolding for packaging microelectronic devices have enabled devices that otherwise would not have been possible using any single technique. Hybridization of microfabrication techniques can potentially permit greater material selection, allow complex and truly three-dimensional structures with high aspect ratios, and offer greater integration of structural, mechanical, and electronic components.

1.4 Project Goals

The work presented in this paper aims to explore the usefulness of several hybrid microfabrication techniques through the creation of various microelectrode array types. A series of hybrid microfabrication processes were investigated to determine the ability to create novel structures using common manufacturing processes including photolithography, MEMS fabrication techniques, precision tool-based micromachining, microwire assembly, micromolding, embossing, and electrodeposition. These experiments were exploratory in nature and microfabrication processes showing promise were pursued to develop a baseline for further investigation but not optimized for performance. The microfabrication investigations are presented in chronological order for which the work was conducted. The three major elements of this project include: 1) the use of tool-based micromachining, microwire assembly, molding, and electrodeposition to fabricate a microwire shank MEA, 2) the use of wet etching, micromolding, embossing, lapping, and lithography to control light transmission through optical

fibers for optogenetic microelectrode applications, and 3) creation of a flexible microelectrode array from a biocompatible polymer using MEMS and photolithographic techniques. These three projects demonstrate several hybrid microfabrication techniques that enable complex structures and geometries, offer a wide material selection, and allow improved integration over traditional microfabrication techniques.

CHAPTER 2: HYBRID MICROWIRE MICROELECTRODE ARRAY

2.1 Introduction: Microelectrode Arrays

The two main MEA types presented here were developed for either recording electrical neural activity in the brain or electrically stimulating nervous tissue. All MEAs described are intended for implantation into nervous tissue and are thus designed to minimize adverse tissue response and provide high quality recording and stimulation. Adverse immune responses to implanted electrodes are caused by insertion trauma, foreign body response to the electrode material, or micromotion of the electrode [5]. The MEAs include sharpened tips to facilitate penetration into nervous tissue and flat sides to reduce insertion trauma to surrounding tissue. All components of the electrodes are manufactured with biocompatible materials that minimize toxic or necrotic response in tissue and provide reduced immune and foreign body responses. The electrode shanks are designed to be mechanically stiff enough to endure handling and implantation, but flexible enough to minimize tissue damage by complying with micromotion between the implant and the surrounding tissue [7]. Anodically electrodeposited iridium oxide film (AEIROF) is electrochemically deposited on the gold electrode sites to decrease impedance and increase charge-injection capacity of the small-area electrodes on the MEA [31].

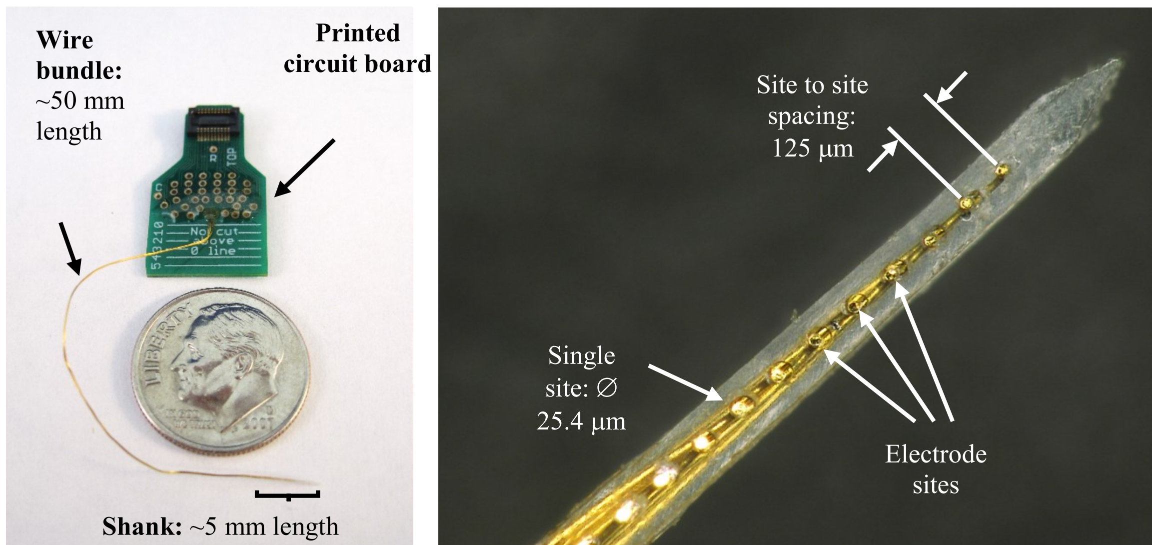

Figure 2.1 Microelectrode Array Overview. The recording shank MEA contains 32 channels with 125 µm spacing with an overall shank length of 5 mm. A 5 cm wire bundle connects the shank to the interfacing PCB.

The MEAs described consist of a shank, a wire bundle, and a printed circuit board (PCB). The shank comprises multiple microwires encapsulated by a clear biocompatible polymer and provides multiple AEIROF recording sites along its length. The wire bundle, 50 mm in length and consisting of one gold microwire for each channel in the device, connects the shank to a two-sided PCB that contains a mating connector for interfacing with a ZIF-Clip ZC32 headstage (Tucker Davis Technologies, Alachua, FL).

The recording electrode was designed specifically for implantation into the inferior colliculus (IC) of the feline midbrain and features 32 circular AEIROF plated electrode sites with 25.4 µm diameter spaced at 127 µm intervals. The rectangular profile shank is 5 mm in total length with uniform thickness of 127 µm and width tapering from 250 µm at the base to 127 µm at the tip. The tip of the electrode is sharpened with an included angle of 30° to facilitate penetration through the *pia mater* and into the IC.

The stimulating electrode features 16 rectangular stimulation sites spaced at 150 µm intervals. Each electrode site consists of a 75 µm wide rectangular band that wraps around the

electrode shank. The 3 mm long shank of the stimulating electrode is 100 μm wide at the base and tapers to 50 μm wide at the tip. It has a tapering thickness from 100 μm to 50 μm to maintain a square shank profile. The stimulating electrode has a sharpened stimulating site at the tip which serves as an extension of the penetrating tip of the MEA shank. The overall length of the wire bundle from the base of the array to the PCB is 10 cm.

2.2 Microfabrication of Shank Microelectrode Arrays

The hybrid fabrication of the MEAs involved adapting multiple processes from established precision microscale fabrication methods. Modern computer numerical controlled (CNC) machines capable of micrometer-level tolerances and were used to create the shank molds, planarize the electrode sites, and sharpen the tips of the MEAs. Assembly of microwires into shank molds was performed manually under low magnification via stereoscopic microscope. Micro scale molding and sacrificial release were used to cast and later release the MEA shank as well as provide a fixturing solution during post processing and machining. The combination of technologies such as machining, molding, electrochemical deposition, and sacrificial release enables unique geometries, improved materials selection, and provides the flexibility to incorporate new technologies and materials as they become available.

Mold precursor workpiece mounting holes and outlines were etched with a CO_2 laser cutter (VersaLaser VL-200, Scottsdale, AZ) onto a 381 μm (0.015 in) thick Poly(methyl methacrylate) (PMMA) sheet (SABIC Polymershapes, San Diego, CA). The workpieces were etched as opposed to fully cut because the ablation process used by the CO_2 laser to cut PMMA causes warping around the edges of the substrate surrounding the cut. Because of the multiple fixture transfers and micrometer tolerances required during the hybrid manufacturing process, it is necessary to minimize all sources of deviation in part tolerance. The CO_2 laser power was

decreased by 30% before etching the mold workpiece in order to avoid the burrs created from the molten material, and the workpieces were mechanically separated from the bulk material. Mold workpieces were mounted to an aluminum machining fixture and securely fixed onto the bed of a Haas vertical CNC Mini Mill (Haas Automation, Oxnard, CA) for machining of the mold features.

The quality of the machined cuts in the PMMA molds determines the surface finish of the electrode shank that is cast in the PMMA molds. With traditional machining procedures, multiple equations are used to determine the optimal spindle speed, cutting rate, and material removal per pass based on the tool's diameter and number of flutes and properties of the substrate material. However, with tools smaller than 0.01" and with nonmetal substrate materials, these formulas rapidly break down and lose relevance as they produce impossible outputs. For example, a two flute square end mill with a 0.002" (50.8 μm) diameter cutting PMMA with a recommended cutting speed of 500 surface feet per minute would require a spindle speed of nearly one million RPM (954,930 RPM) and a feed rate of 954 inches per minute, parameters which are unachievable with current machines. In addition, polymers are notoriously difficult to machine as compared with metals because they exhibit very high levels of thermal expansion, lose heat very slowly, possess low softening and melting temperatures, and are highly elastic. In order to achieve the highest quality finish on the machined PMMA electrode shank molds, the parameters of spindle speed, feed rate, tool geometry, cut depth, and number of finishing passes to create these molds were optimized through empirical testing.

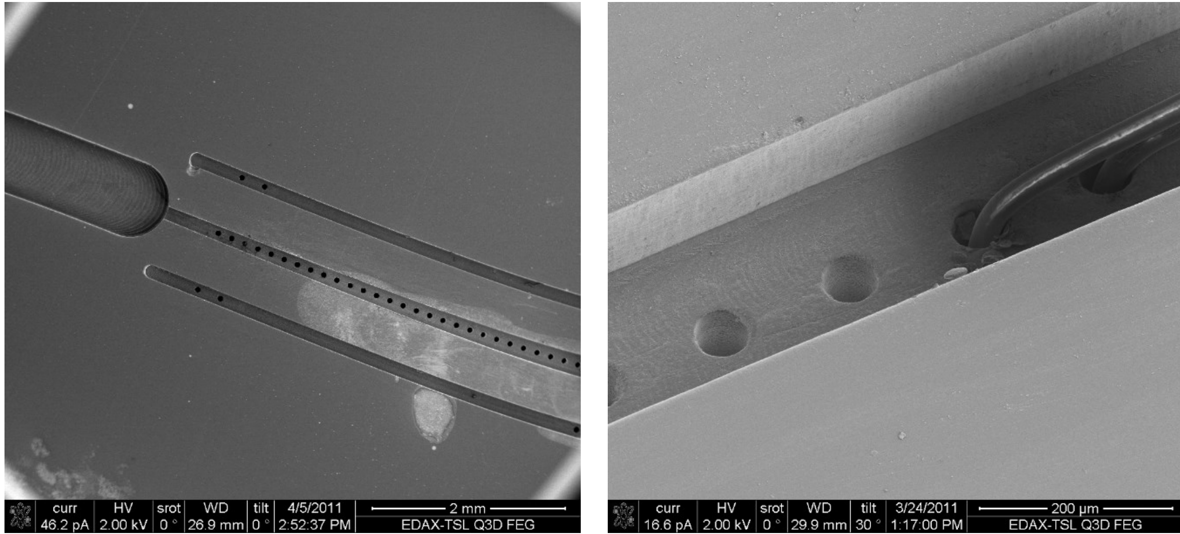

Figure 2.2 SEM of PMMA Micromolds. Molds were fabricated on a CNC vertical mill with feed rates lower than 2.5 mm/min and 6,000 RPM spindle speed. The central slot is 127 μm deep and tapers from 250 to 127 μm wide. A 25 μm microwire is shown inserted into a 50 μm diameter hole.

The slotted mold features were machined using two-flute miniature carbide square end mills having diameters 50.8 μm (0.002 in), 76.2 μm (0.003 in), and 127 μm (0.005 in) (Microcut Inc., P/Ns 82002, 82003, 82005, Kingston, MA). All cutting tools were rotated at the machine's 6,000 RPM maximum and fed into the material with both plunging and contour cutting feed rates dictated by empirical testing, ranging from 0.2 - 1 in/min. Each cutting pass removed substrate material equal to 20% of the tools diameter.

The through-holes in the molds were drilled at 6,000 RPM with a 50.8 μm (0.002 in) diameter drill (McMaster-Carr, P/N 8904A11) using a peck drilling cycle. The drill was fed into the stock material at a feed rate of 15.24 mm/min (0.6 in/min) in passes of depth 25.4 μm (0.001 in) until the drill passed completely through the mold material. Following the completion of all drilled holes, the drill was fed through each hole in order to remove excess material that had accumulated in the holes.

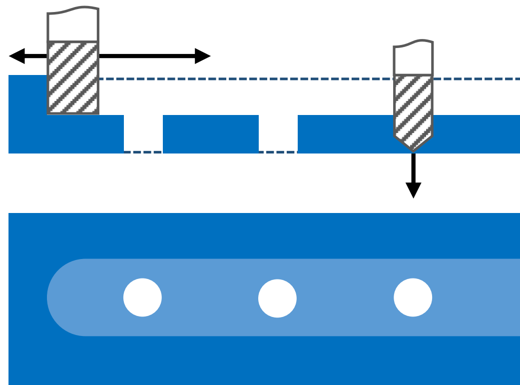

Figure 2.3 Diagram of Micromold Milling and Drilling Operations.

To facilitate attachment to fixtures later in the assembly process, alignment holes were drilled in the mold with a 5/64" spot drill followed by a #52 drill (1.613 mm) (McMaster-Carr, P/Ns 2925A54, 8903A67). A 0.8 mm wide reservoir for holding and dispensing casting epoxy was machined as a 127 μm deep slot at the tip end of the shank slot (McMaster-Carr, P/N 8876A28). All milling operations were performed under a pool of machining oil to improve chip clearance and surface finish.

The molds were cleaned of debris and oils by first rinsing in isopropyl alcohol (IPA) and distilled (DI) water, then suspending in an ultrasonic cleaner filled with DI water for 15 minutes, followed by a final IPA and DI rinse. The molds were dried with pressurized air and set in the oven to dehydrate for 2 hours at 85°C. The cleaned and dried molds were mounted to an assembly fixture with adjustable PCB clamping locations to allow adjustment for wire bundle length.

Sections of polyurethane insulated 50 AWG (25 μm) Gold microwires (California Fine Wire, Grover Beach, CA) 15 cm in length were threaded into the molds by hand under low magnification. The wire ends were affixed to double-sided tape on the backside of the fixture and the remainder of the wire was pulled taut into the mold and threaded into the corresponding via hole in the PCB. Electrical connection of the gold wire to the gold pad on the PCB was

established by a thermal-mechanical wedge bond. Often used to make electrical interconnections for the electronics industry, wedge bonding creates electrical connections between a wire and a metal pad through a combination of heating, pressure, and ultrasonic energy [32]. A custom ball-end solder iron tip heated to 400°C was created as a tool to melt the polyurethane insulation from the gold microwires and mechanically bond the gold wire to the PCB. While not a complete wedge bond without ultrasonic energy, the thermal mechanical bonding of the gold wires to the PCB pads provides sufficient bonding to produce reliable electrical connection. Electrical conductivity was tested across each pad and wire post wedge bond, and each successful bond was coated with epoxy to provide strain relief to the joint.

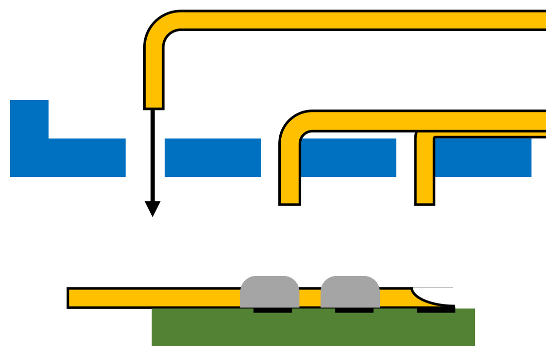

Figure 2.4 Diagram of Microwire Threading and Thermal Mechanical Bond Processes. Wire ends are threaded into through-holes in the PMMA molds. The opposite wire end is connected to PCB via thermal mechanical bond with a gold plated PCB pad. Successful bonds are coated with epoxy as stress relief.

An epoxy resin was cast into the mold containing the microwires to consolidate the wires into a single shank. EPO-TEK 301, a nontoxic epoxy, was selected due to its compliance with USP Class VI Biocompatibility standards and very low viscosity of 100-200 cPs at 100 RPM/23°C (Epoxy Technology, Billerica, MA). EPO-TEK 301 was mixed in a 4:1 ratio by weight and injected into the mold reservoir with the assembly fixture held at a 45 degree angle to prevent the epoxy from entering the mold. The fixture was placed under vacuum and laid flat to allow the epoxy to fill the mold cavity via capillary action. Once filled, the mold was removed from vacuum and transferred to a 40°C oven overnight for the epoxy to cure completely.

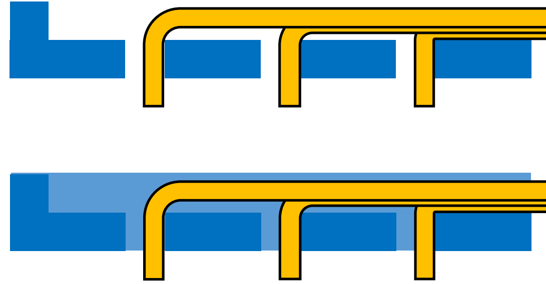

Figure 2.5 Diagram of Epoxy Casting in Micromold. The micromold with assembled wires is filled with EPO-TEK 301 by capillary action.

The mold was removed from the assembly fixture and placed into a secondary machining fixture to allow the wire ends to be cut and the chisel tip to be formed. In the first operation, the mold was placed upside down and attached to the machining fixture. A 127 μm square end mill rotating at 6,000 rpm was centered over each wire end plunged into the backside of the mold in increments of 25.4 μm with a feed rate of 1 in/min. The end mill was plunged to the depth of the epoxy shank to remove excess mold material, wire, and casting epoxy and planarize the electrode shank. This process exposes the gold microwire cross sections that become the electrode sites after release of the electrode from the PMMA mold. In the second operation, the mold was flipped over and reattached to the machining fixture. A 0.8 mm square end mill was used to cut through the mold and epoxy to create a sharp tip on the electrode shank. The end mill was programmed to take multiple 25.4 μm deep passes to achieve a total depth greater than the thickness of the mold to obtain a high quality surface on the sharpened tip.

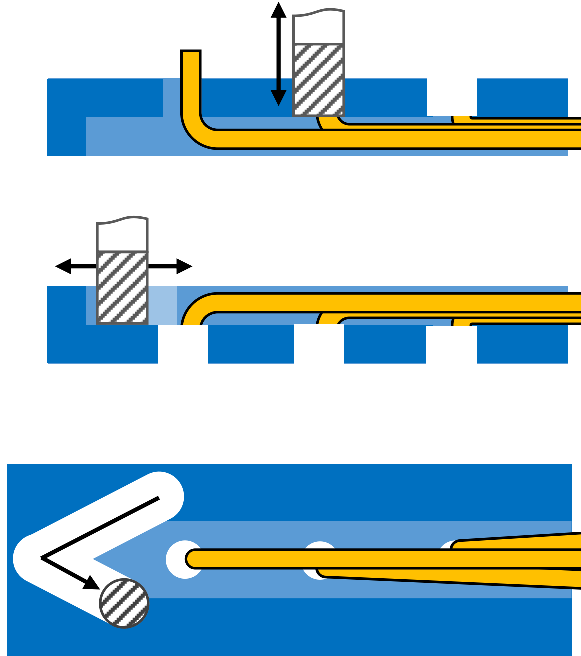

Figure 2.6 Diagram of Wire Trimming and Tip Forming. A square end mill is centered over each wire and removes excess wire, epoxy, and mold material above the specified level in a plunging operation. The same tool is used to cut a beveled tip in the electrode.

The mold with attached electrode was removed from the machining fixture after shaping the tip and removing the excess wire. Because of the fragile nature of the electrodes, a mechanical release of the electrode shank from the PMMA mold was abandoned in favor of a sacrificial chemical release method. To this end, PMMA was selected for the mold material because it exhibits a high level of rigidity and machinability and solubility in acetone. The excess PMMA mold material surrounding the sharpened electrode shank was carefully trimmed with shears to within 1-2 mm of the shank. The trimmed PMMA mold and electrode were submerged in acetone at 23°C and inspected at thirty minute intervals until the remaining PMMA mold material was completely dissolved from the electrode shank. The electrode was rinsed with fresh acetone, IPA, and finally rinsed in DI water to remove any remaining PMMA and surface debris.

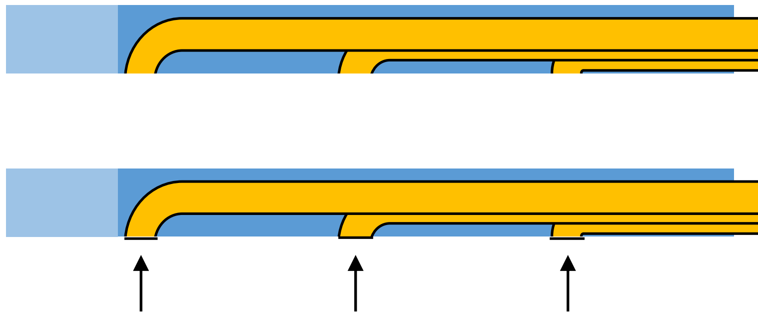

Figure 2.7 Iridium Oxide Deposition on Exposed Wire Ends.

The exposed gold wire sites were coated with an anodically electrodeposited iridium oxide film (AEIROF) to allow for optimal current and charge density and avoid electrochemical reactions that degrade the electrode or cause damage to surrounding tissue from harmful by-products [33]. Prior to coating with an AEIROF, the exposed gold sites were first conditioned to remove surface debris and add texture to the electrode sites. The electrode was submerged in a 0.9% NaCl solution at 23°C and a 1 kHz 2.8V peak-to-peak sine wave was applied across a platinum electrode to each channel for 2 seconds. This adds texture to the gold sites and significantly increases their surface area.

Iridium oxide was plated on the conditioned gold sites using a similar protocol as described by other groups [33]. An aqueous solution of 4 mM $IrCl_4$ was combined with an electrolyte solution of 40 mM oxalic acid and 340 mM K_2CO_3 with a final pH of 10.5. Under potential control from a potentiostat (Digi-Ivy DY2013, Austin, TX), a three cell system was setup in the iridium oxide solution with the MEA as the working electrode, a platinum wire counter electrode, and a 1M KCL silver/silver chloride (Ag|AgCl) reference electrode. First, a triangular waveform ramped from -0.025 V and 0.525 V at a scan rate of 50 mV/s was applied for 50 cycles to improve adhesion of the AEIROF coating. Immediately following this step, a

rectangular waveform which cycled between -0.025 V and 0.525 V potential held for 0.5 seconds was applied for 1600 iterations in order to produce the AEIROF coating.

2.3 Electrode Characterization

Electrodes can be characterized in vitro by their impedance characteristics and cyclic voltammetry response. Electrode impedance is an indicator of the effectiveness of an electrode in recording single-unit action potentials. Cyclic voltammetry (CV) is a measurement used to identify the presence and reversibility of electrochemical reactions, the amount of available electroactive material, and the stability of an electrode [5], [34]. These measurements can be applied in vitro and are representative indicators of the MEAs performance in vivo. The results of these measurements are presented in the following section.

With the goal of measuring single-unit neural action potentials in a chronic experiment, an effective MEA should provide a signal to noise ratio of 5:1 or greater [5]. Action potential amplitudes in feline auditory cortices typically range from tens to 100 μV [35]. A large source of signal noise in intracortical single-unit recordings stems from neuronal noise, or background action potentials in the vicinity of the electrode. Another source of signal noise is electrode impedance, and a higher impedance electrode will generally result in a lower signal to noise ratio. The wedge bond connection and the surface of the electrode sites were identified as potential sources contributing to total device impedance.

The wedge bond impedance was measured across two bonds of a gold microwire. A segment of the polyurethane insulated gold microwire used in the manufacture of the MEAs was bonded at 400°C across two copper pads of the PCB in an identical fashion as during fabrication of the MEAs. The impedance was measured across equidistant pairs of pads at 1 kHz and 250 mV. Over 18 recordings tested, the wedge bonds had average impedance 0.60 ohms with a

standard deviation of 0.02 ohms. The impedances resulting from the capacitive double layer at the electrode/tissue interface range from kOhm to MOhm. The elevated impedance at the electrode sites far outweighs the impedance component resulting from the thermal mechanical bonding of wires to the PCB, and this bonding method was deemed appropriate for effective electrical connection.

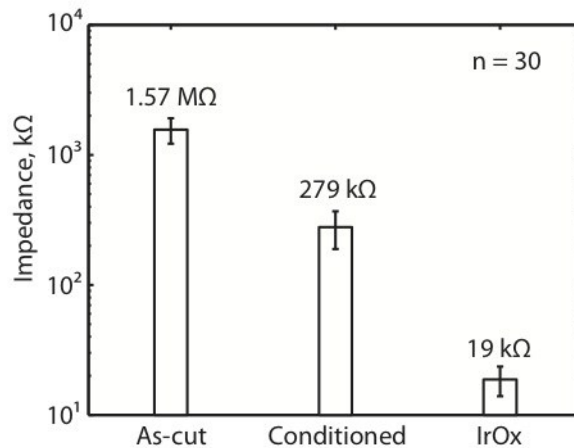

Figure 2.8 Average Impedance for As-cut, Conditioned, and IrOx Plated Electrode Sites.

The electrode site impedance was measured at three critical points during the fabrication process: after trimming of the gold microwires, after cleaning and conditioning the gold sites, and post AEIROF plating. All electrode site impedance measurements were recorded against a platinum wire in 0.9% NaCl at 23°C using an impedance meter (B&K Precision, Model 885, Yorba Linda, CA) at 1 kHz frequency and at 250 mV. The as-cut gold microwires, conditioned gold sites, and iridium oxide coated sites displayed average impedances of 1.57 MΩ, 279 kΩ, and 19 kΩ, respectively. This significant decrease in impedance can be explained by the increase of electrochemical surface area (ESA) relative to the geometrical surface area (GSA) of the as-cut electrode sites. The GSA of the 32 channel recording electrode using 25.4 μm diameter wire was calculated as 506 μm^2 using the methods described in [36]. The charge

transfer between the electrode and tissue is dominated by a capacitive metal double layer in which a layer of water molecules and a secondary layer of hydrated ions form capacitive inner and outer Helmholtz layers [9]. The ESA is directly proportional to this capacitance and can be calculated from the impedance measurements taken. Based on these calculations, it is estimated that the ESA of the conditioned gold sites is nearly six times greater than the bare gold sites. The apparent texture added by the gold conditioning process as seen in SEM of As-cut, Conditioned, and IrOx plated sites., appears to qualitatively confirm an increase in surface area. AEIROF layers are characterized by a highly porous structure, with oxide grains 0.05-0.1 μm in diameter, a high density of macro voids 0.05-0.07 μm in diameter, and microvoids ~25Å in diameter [37]. The porous AEIROF layer deposited over the conditioned gold further increases the ESA of the electrode sites, explaining the final decrease in electrode impedance.

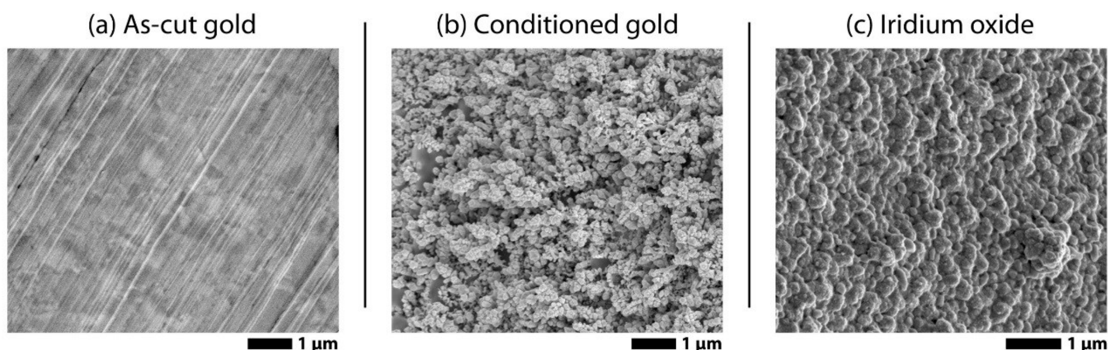

Figure 2.9 SEM of As-cut, Conditioned, and IrOx plated sites.

The AEIROF coated electrodes were subjected to a three-electrode potentiostatic CV measurement involving the MEA, a constant potential reference electrode, and a counter electrode. The potential of the MEA with respect to the reference electrode is swept cyclically between two potentials at a constant rate. The current flow measured between the MEA and counterelectrode is proportional to the rate constant of the electrochemical reactions created by the potential sweep [38]. CV measurements were performed at room temperature in

deoxygenated phosphate-buffered saline (PBS) solution containing 0.13 M NaCl, 0.022 M NaH_2PO_4, and 0.081 M Na_2HPO_4 with pH ~7.3 [20], [31]. An Ag|AgCl electrode and large area platinum wire were used as the reference and counter electrode, respectively. The working electrode was configured by connecting all channels of the MEA into a single electrically conductive unit with a modified connector. Cyclic voltammograms were obtained with a potentiostat (Digi-Ivy DY2013, Austin, TX) by cycling the potential between the working and reference electrode from -0.6 V and 0.8 V at a scanning rate of 50 mV/s [33]. The potential limits used in the CV measurement represent in vivo stimulation limitations and are based on the upper and lower limits of the water electrolysis window for iridium oxide.

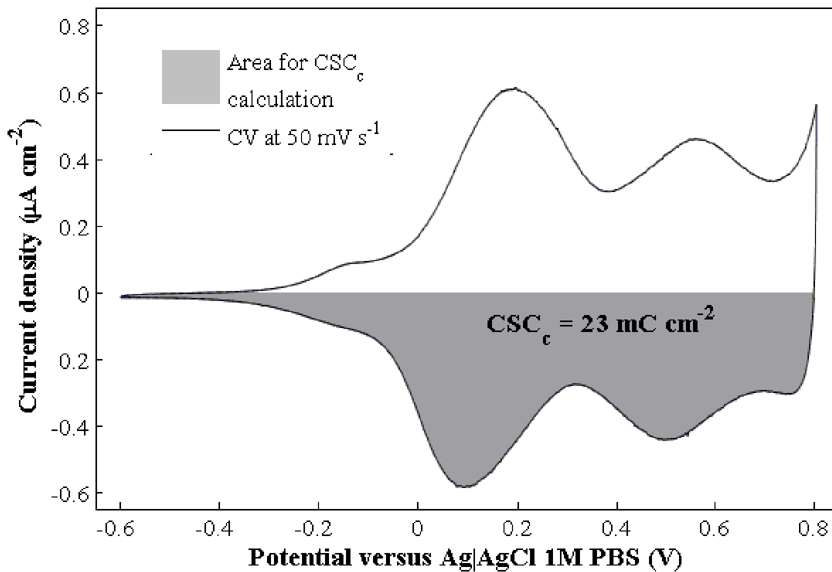

Figure 2.10 Cyclic Voltammogram of IrOx Plated Electrode Sites.

A typical AEIROF CV result is presented in **Error! Reference source not found.**. The ime integral of the cathodic current, illustrated by the shaded region, is used to calculate the cathodal charge storage capacity (CSC_C) of the electrode. The CSC_C, is often used as a measure of the maximum total charge available for a stimulating pulse, and the calculated value of 23 mC cm^{-2} corresponds with the expected CSC_C of an iridium oxide electrode [33]. The rectangular

shape of the CV plot represents the capacitive double layer formed at the electrode surface, and the non-adsorptive faradaic processes indicated by the peak separation confirm the presence of an iridium oxide layer with electrochemical properties consistent with commercially available silicon and microwire MEAs [20], [33], [39].

2.4 Microelectrode Array Configurations

One limitation of linearly arranged stimulation sites is the requirement that the active electrode side of the shank be precisely oriented with respect to the tissue of interest. If improperly implanted, the stimulation sites may be 180 degrees out-of-sync with the targeted tissue. Additionally the site-to site spacing, and therefore specificity, of the MEA is limited with electrodes oriented linearly on a single side of the MEA shank. Recording MEAs with excessively close electrodes suffer from crosstalk. A multi-sided MEA that contains electrodes on more than one shank face addresses several of these problems. Altering the electrode placement circumferentially on the shank allows for stimulation of tissue along 360 degrees of tissue surrounding the MEA shank. For recording electrodes, the number of sites per shank length can be increased, resulting in higher resolution recordings in neural tissue with little change in shank size.

A major advantage of tool-based micromachining is the ability to add, substitute, and modify processes and rapidly adapt to new fabrication strategies. The hybrid microfabrication techniques used to fabricate the shank MEA above benefit from this ability and to illustrate the inherent flexibility of the hybrid microfabrication process, a shank MEA was created with electrode sites along three sides of the shank. Several key fabrication steps are shown in **Error! eference source not found.**. The molds were modified to include slotted features for wires to exit the mold along the sides in addition to the bottom of the mold channel. The machining tools

and mold substrate material were unchanged and only slight modification to the machine tool paths was necessary. Once completed, gold microwires were assembled into the modified PMMA molds and epoxy was cast into the mold under vacuum. The wire ends were removed and the tip of the electrode was shaped in the machining process described above, and an additional machining step was added to remove the wire ends along the sides of the electrode shank.

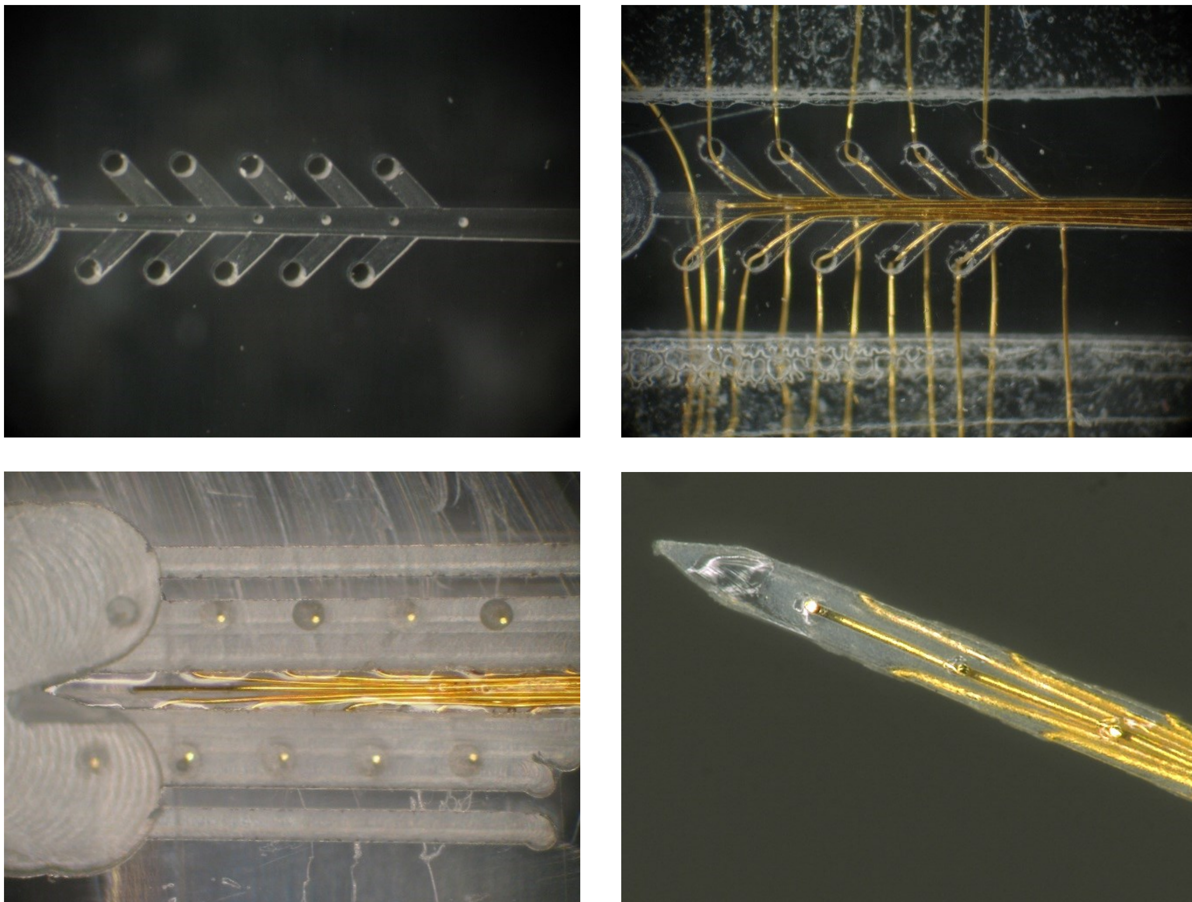

Figure 2.11 Three-Sided MEA. Shown are the PMMA micromold, micromold assembled with 25 μm wires, post casting machining of wire ends and tip, and completed electrode after sacrificial release.

The hybrid manufacturing approach offers great flexibility in the modification of MEA designs, providing a significant advantage over lithographically fabricated or microwire MEAs. Minor modifications to lithographically produced electrodes requires the creation of entirely new

photomasks and leads to increased processing time, expense, and lower yield whereas the hybrid approach allows electrode shank materials, surface treatments, electrode size, and site number and position to be rapidly and easily added, substituted, or modified without disrupting subsequent fabrication steps.

2.5 Increasing MEA Surface Area

One major challenge faced with the design of stimulating microelectrodes is balancing stimulation efficacy with safety. The charge/phase injected into the target tissue must surpass a stimulation threshold, but is also limited by a maximum charge potential in which irreversible electrochemical degradation of the electrode occurs and toxic by-products are released into nearby tissue [7]. The high charge densities required by microelectrodes with small stimulation site surface areas can contribute to faradaic reactions on the metal electrode which result in electrode degradation and tissue damage [40], [41]. It is possible to decrease the charge density of an electrode by increasing the geometrical surface area of the electrode sites, but a loss of specificity occurs when the electrode sites become excessively large. Several methods for increasing the geometrical surface area of the shank MEA sites by utilizing the multiple sides of the electrode shank were investigated, with the additional goal of maintaining site spacing and therefore specificity of the electrode array.

In the previously described design, each electrode stimulation site is defined by the cross-sectional area of the gold microwire, but by depositing metal bands circumferentially around the electrode shank and encapsulating the existing electrode sites, the surface area of the electrode may be significantly increased without increasing site to site spacing or altering the size of the electrode shank. An additional benefit of decoupling the wire diameter from geometrical surface area is a potential decrease in shank diameter. In the MEAs presented here, the shank diameters

are determined by the number and diameter of the microwires used in their construction. Using smaller diameter wires would permit smaller diameter shanks to be made, and metal banding over these wires could provide GSA equivalent to shanks made with larger microwires. The ability to decrease the shank size of a microelectrode without sacrificing performance represents a significant advantage in microelectrode fabrication.

Photolithography is often used to create metal microstructures through either subtractive or additive processes. Subtractive processes are performed on substrates that have been uniformly coated with a basement layer of metal. A light sensitive photoresist is patterned on the metal surface and serves as a chemical barrier while the exposed metal is removed by submersion in an aqueous etchant. Additive methods control the deposition of metal by mechanical means. Metal is uniformly coated over a patterned stencil and is deposited on the substrate in unmasked areas. Traditionally, these processes are enabled by two-dimensional photomasks that create positive and negative space in which photoresist can be patterned onto the planar substrate via a collimated ultraviolet light source.

While most lithographic processes are performed on planar substrates with high levels of flatness, the major obstacle in patterning metal structures on a non-flat substrate such as an MEA shank involves accurate fixturing and precise alignment of the photomask. In order to utilize lithographic processes on a non-planar three dimensional substrate such as an electrode shank, an alternative method of photomasking was investigated. A precision machined metal stencil was created to enable the lithographic formation of metal bands on the non-planar electrode shank. Because effective photoresist exposure is an essential component of this method, a milestone of this investigation was demonstrating the ability of both negative and positive resists to be patterned via stencil on a cylindrical or other three dimensional substrate.

Metal band formation by subtractive etching was demonstrated on cylindrical substrates. Initial design dictated that the electrode shank would be dipped into a thinned/diluted photoresist solution, soft-baked until dry, then placed into the 3D photomask and exposed and developed. In order to create bands that surround the circumference of the MEA shank, the electrode would be rotated ninety degrees and the process repeated. An underlying layer of metal would be chemically etched in the exposed regions and the photoresist removed, leaving metallic bands around the MEA shank.

First, the ability to pattern photoresist on cylindrical substrates was explored. Cylindrical rods were formed from the same epoxy used to cast the MEA shanks by injecting the uncured epoxy into silicone tubing with an inside diameter of 1 mm. The epoxy was cured under normal conditions and released by cutting away the tubing. In the first iteration of stencil design, a copper tube with inside diameter > 1 mm was manually machined with a 0.125 in square end mill by running the end mill perpendicular to the tube axis in a partial-depth cut. The positional accuracy, feed rate, and material removal per pass were poorly controlled as the machine tools were fed into the copper tube substrate manually. The epoxy substrate was dip coated in positive photoresist by plunging into a container of resist and removing at a constant rate to achieve an approximately uniform coating, then soft baked at 65°C to drive off solvents. The resist coated epoxy rod was inserted into the lumen of the copper stencil and exposed to ultraviolet light, rotated 180° inside the stencil and exposed again, and finally removed and developed. As seen in **Error! Reference source not found.**, the preliminary test was successful in showing the bility to pattern photoresist in banded shapes on a large diameter cylindrical substrate. The rough boundaries of the photoresist pattern is attributed to scattering of UV light caused by the

poor surface quality of the edges of the stencil and the relatively large distance between the stencil and the photoresist.

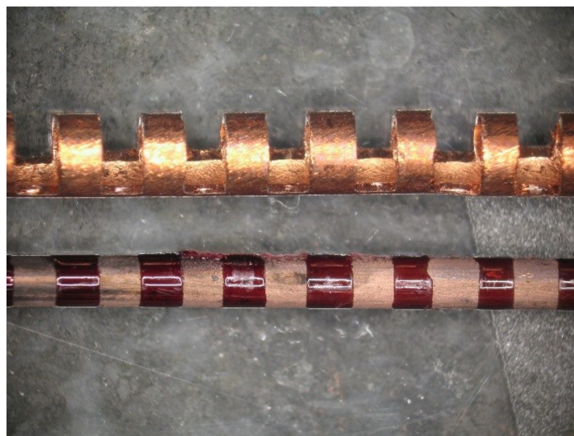

Figure 2.12 Preliminary 3D Lithography Stencil and Resulting Structure.

Scaling down the size of the stencil and substrate was determined to be the next critical step in creating bands on the MEA shanks. Precision miniature stainless steel tubing (McMaster-Carr, P/N 8988K72) was cut using a vertical CNC Haas Mini mill to create negative space for exposure to UV light and other line-of-sight processes. The cuts performed on the tubing ranged from 0.003” (75 µm) to 0.005” (125 µm) with a cut depth of 0.015”. It was observed that as the depth of cut increases, the rigidity and therefore positional accuracy of the three dimensional mask suffers. Too shallow of a cut results in an aperture that is too small for the UV light to enter the stencil. Because the machined edges define the quality of the stencil, great emphasis was placed upon surface quality of the cut faces, but machining parameters were not yet optimized during these tests. The machined molds are shown in **Error! Reference source not found.**.

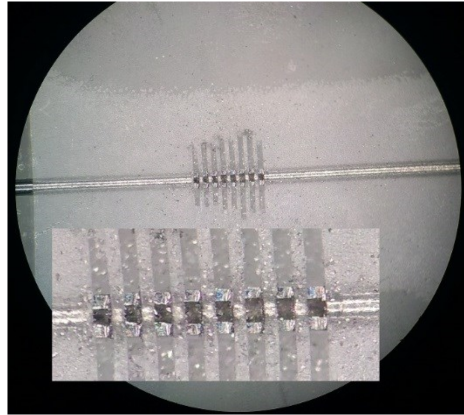

Figure 2.13 Machined 3D Lithography Stencil

Preliminary tests with the updated stencils were performed on cylindrical substrates. Non-insulated copper wire was initially used to test photoresist patterning ability due to its low cost, ease of handling, and high cylindrical tolerances. Photoresist was patterned on a size 11 AWG copper wire using the same dip coating and exposing methods used in the larger model. Photoresist bands with an approximate 1:1 open/closed ratio were replicated with reasonable fidelity on the wire, and can be seen in **Error! Reference source not found.**. To determine the bility of the patterned photoresist to function as an etch stop for subtractive processes, a metal coated optical fiber was used in place of the wire to assist in visualizing the removal of metal after etching. A 125 μm diameter optical fiber was subjected to an electroless copper plating process (PC Electroless Copper, Transene Company, Inc., Danvers, MA) and a 5 μm thick copper layer was deposited over the entire fiber. The optical fiber was dip coated in photoresist and patterned using the metal stencil. The patterned metal coated fiber was submerged in an ammonium persulfate copper etchant solution to etch the exposed metal. The photoresist was stripped in acetone, leaving the patterned metal structures seen in **Error! Reference source not ound.** d).

The ability to create more robust metal structures was illustrated by including an additional metal deposition step adapted from electroforming and sacrificial molding techniques.

Patterned photoresist was used as a sacrificial mold and copper was electrodeposited into the negative space before stripping the photoresist. After photoresist was patterned on the fiber, electrical connection was made to the underlying metal layer in order to build up the exposed metal layer through DC electroplating of copper. Copper was deposited at a rate of 0.5 mil/hour under a 5V potential bias in a prepared copper electroplating solution (Copper Plating Acid Type, Transene Company, Inc., Danvers MA). Electroplated copper thicknesses on the order of 10-100 μm were deposited over the exposed copper seed layer using this method. The photoresist served as a physical barrier to the electroplating process and was stripped from the fiber post-plating. The fiber was placed into a diluted etchant solution until the metal seed layer was completely removed. This created the taller bands seen in **Error! Reference source not ound.** c).

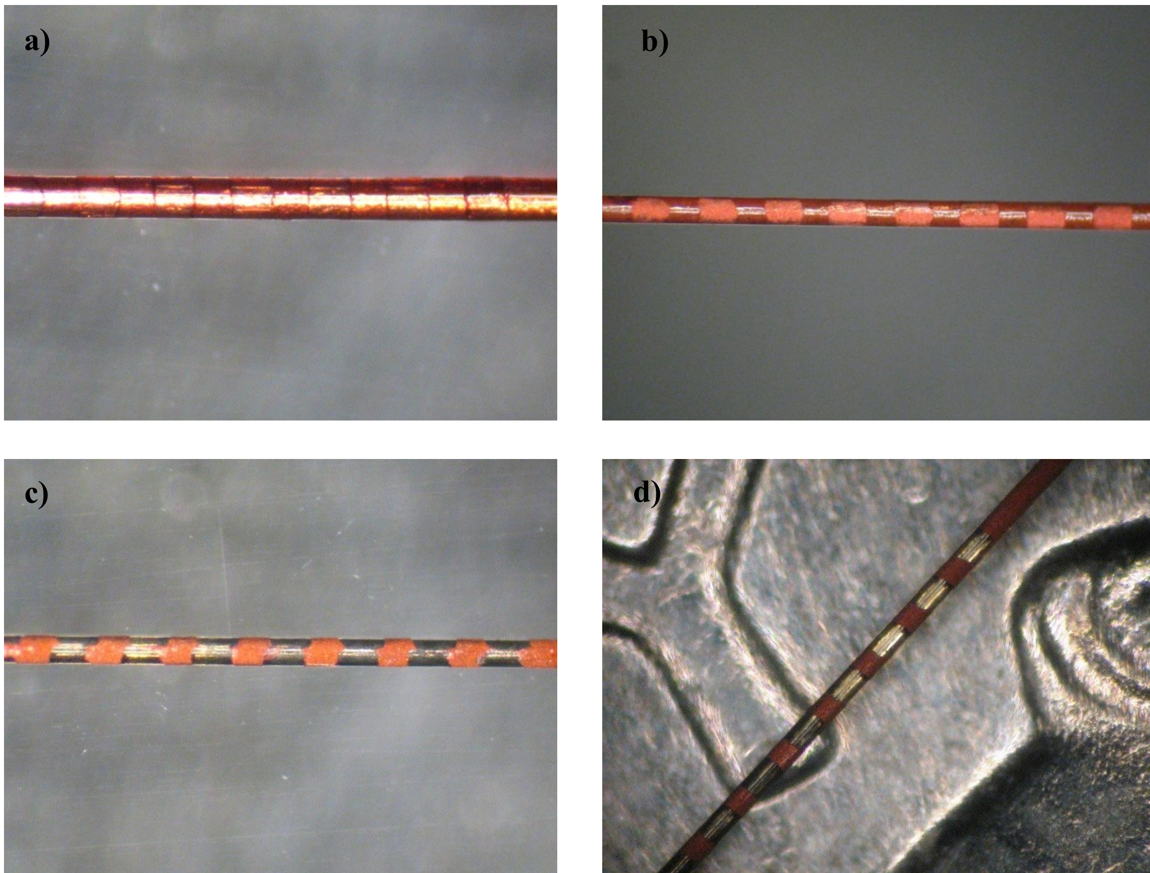

Figure 2.14 3D Patterned Optical Fibers. 125 μm diameter optical fibers plated with copper and subjected to the 3D lithography process. (a,b) Optical fiber dip coated with photoresist, exposed using 3D stencil, and developed, shown before stripping photoresist. (c) A DC electroplating process was used to build the metal thickness of the deposited bands. (d) A fiber after etching the exposed copper and stripping the remaining photoresist. Seams in the metal bands that are the result of lateral movement while rotating the fibers between UV exposures can be seen.

As a final test of the ability to pattern metal bands on non-cylindrical substrates, metal bands were directly deposited on electrode shank phantoms using evaporative depoisition. One distinct advantage of the stencil mask over a traditional lithographic hard mask is the ability to function directly as a metal deposition mask for line-of-sight processes such as electron beam physical vapor deposition (EBPVD). EBPVD is compatible with a large number of metals and substrates, as it uses electron bombardment to vaporize the metal to be deposited in a vacuum and condenses that metal on a substrate that is held at a low temperature. EBPVD was used to directly pattern metal on the electrode shank using the stencil as a physical barrier. Electrode phantoms were created by casting epoxy in shank molds that were partially populated with gold

microwires. The phantoms were inserted into stencils, fixed in place, and subjected to EBPVD of titanium over the stencil and electrode. Optical micrographs of the resulting structures are displayed in **Error! Reference source not found.**. The stencil is used to directly control the eposition of the evaporated metal particles, thus eliminating the need to coat the substrate with metal, pattern photoresist, etch the metal layer, and strip the photoresist. While the current method of stencil creation by tool-based micromachining is limited by the diameter of a machine tool, effective stencils with complex geometries can be produced using alternative microfabrication methods. The metal was selectively deposited on the shank in negative areas of the stencil, and various band widths and gaps between were formed.

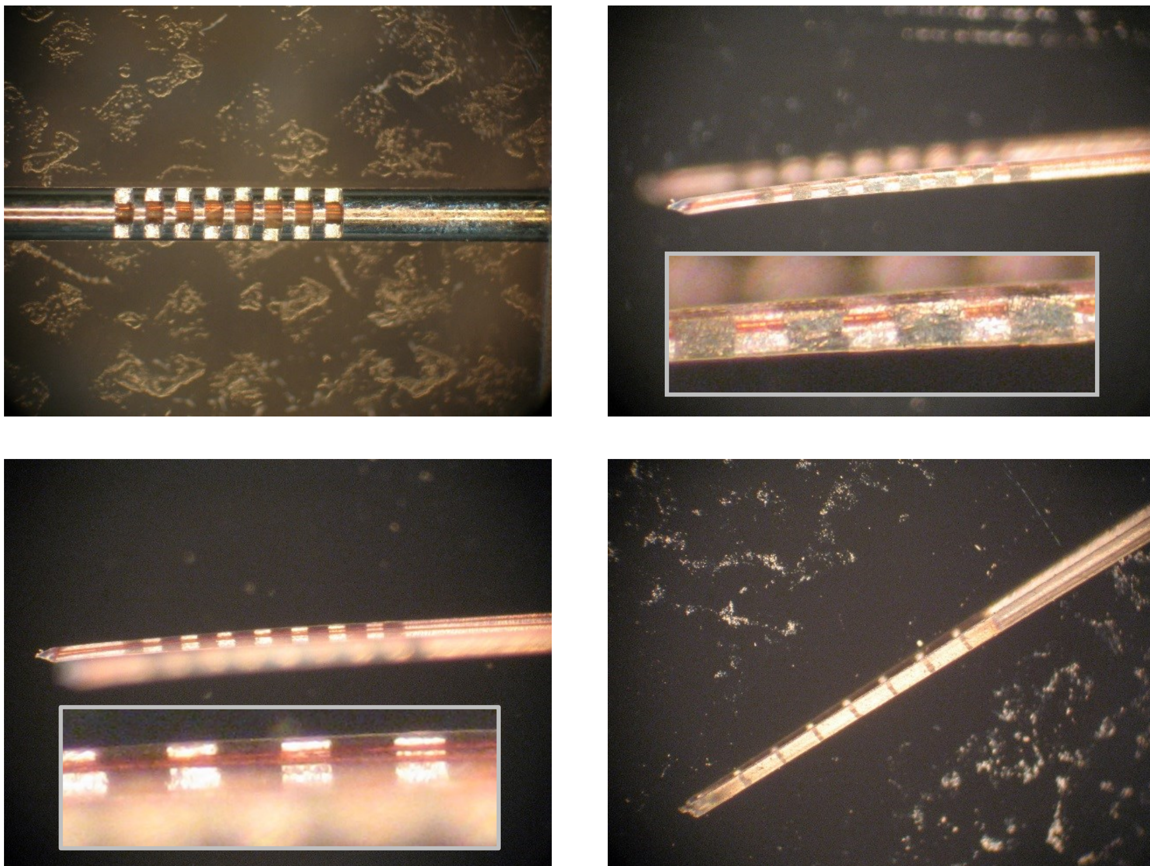

Figure 2.15 Evaporated Metal Bands on Electrode Phantoms. (a) Electrode shank in 3D lithography stencil prior to metal deposition. (b) Electrode shank after metallization. Titanium bands are present on two surfaces of the electrode phantom. (c) Viewed from behind, an embedded microwire is seen occluding the backsides of the deposited bands. (d) Bands resulting from an alternate stencil geometry.

This test was valuable for establishing the feasibility of lithographically patterning metal bands on microscale substrates beyond simple cylinders. Cylindrical and rectangular substrates were successfully patterned with metal bands using both additive and subtractive lithographic processes. While copper and titanium were used in these experiments, many other metals could be substituted, given that they are compatible with electroless or electrolytic plating or physical vapor deposition processes. Although pattern alignment and feature resolution were not optimal in these experiments, it is recognized that they can be greatly improved in future endeavors by increasing stencil quality and surface finish, minimizing gap distance between stencil and substrate, improving uniformity of photoresist coating, and refining the photolithographic parameters used.

CHAPTER 3: OPTOELECTRODE OPTICAL ELEMENTS

3.1 Introduction: Optogenetics and the Optoelectrode

Optogenetics is an emerging science that allows the precise control of neuronal cells through photostimulation [42]. Genetic incorporation of the light activated ion channels Channelrhodopsin 2 (ChR2) and Halorhodopsin (NpHR) via viral transfection into specific mammalian neuron populations has allowed researchers to activate or silence single action potentials or sustained spiking with millisecond precision [43], [44]. While the necessary wavelength and intensity of light are provided by laser, LED, or mercury or xenon bulb light sources, transmitting light from the source to the tissue *in vivo* is commonly accomplished through optical fiber light guides [45].

An optical fiber is a flexible silica-based fiber that transmits light across its length. Typical multimode optical fibers consist of an inner core ranging in diameter from 50-100 μm, a cladding ranging in diameter from 125 to hundreds of micrometers, and a polymer coating that provides mechanical support to the silica core and cladding. The cladding is manufactured with a lower refractive index than the core, forming a waveguide within the fiber that transmits light axially via total internal reflection. The geometry of the core and cladding as well as the aperture size at the tip define the power handling capabilities and the spread of output light from an optical fiber.

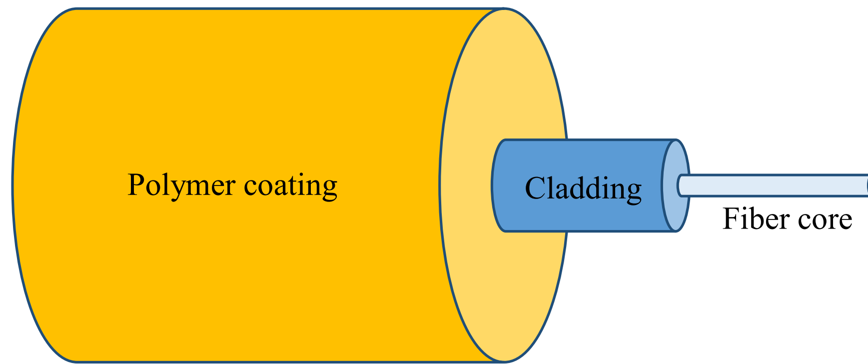

Figure 3.1 Diagram of Optical Fiber Structure

An enabling optogenetic technology is the optoelectrode, a device which serves the dual purpose of stimulating artificially sensitized neurons by delivering light and recording the neural responses evoked by this optical stimulation *in vivo* [46]. Researchers have created optoelectrodes by gluing tungsten electrodes to arrays of optical fibers [47], evaporating metal electrodes directly onto optical fibers [48], [49], attaching optical fibers directly onto silicon MEAs for acute recordings [50], and incorporating waveguide components into silicon MEAs [51].

Despite heightened interest in optogenetics within the last decade, several challenges still exist in fabricating chronically implantable optoelectrodes. Manually attaching a fiber to an electrode shank or electrode array post-manufacturing is inherently imprecise, both in terms of positional accuracy and contamination of recording sites from adhesives [52]. Cleaved flat optical fibers attached to a penetrating shank are mechanically inefficient in terms of insertion forces; significant tissue damage occurs due to the high amount of displaced neuronal tissue [51]. Large diameter silica fibers and monolithic silicon optoelectrodes are inherently rigid and initiate a strong acute immune response upon implantation. It is evident that optical fiber diameter plays a large role in the number of optical stimulation channels available on a single device, the mechanical stiffness of the device as experienced by the tissue, and the penetration forces

involved in device insertion. The geometry of the optical fiber tip is directly related to insertion forces and a shaped or tapered fiber would present less tissue damage than a cleaved fiber tip. Finally, the optical properties of fibers can be manipulated with the addition of chemical additives and shaped lenses to enhance the scattering or decrease the spot size of light exiting the fiber.

Presented in this chapter is a means of reducing fiber diameter by tapering optical fibers, preventing optical loss by metallization of tapered fibers, and controlling light transmission from fibers by creating apertures, focusing lenses, and scattering or diffusing elements on the ends of such fibers. These fiber modifications provide a pathway to a chronically implantable multichannel optoelectrode that incorporates multiple optical fibers with integrated optical focusing and scattering elements.

3.2 Optical Fiber Tapering

The relatively large diameters of optical fibers are a major obstacle in integrating multiple fibers into minimally invasive implantable devices. Coupling optical fibers to a recording electrode causes an additive size increase to the device, resulting in excessive tissue displacement and damage upon insertion. A series of fibers tapered to diameters less than 20 μm could be incorporated into the shank MEA described in chapter 2 without a significant increase in device size. Because of the low power density requirements of stimulating light for activating incorporated opsins (~ 1 mW/mm^2), the diameter of optical fibers can be decreased without sacrificing efficacy in optogenetic applications. The ability to decrease the tip size of optical fibers can lead to greater integration of optical and electrical components in the field of optogenetics.

There are several methods for tapering an optical fiber including drawing, mechanical grinding or polishing, and chemical etching. Drawn optical fiber tapers are created by a combination of heating the fiber with flame to a critical softening temperature and computer controlled pulling of the fiber to control/regulate/govern the taper angle [53]. This process is used to create tapered fiber tips and decreases both the core and cladding diameters uniformly, maintaining the waveguide properties of the optical fiber through the taper.

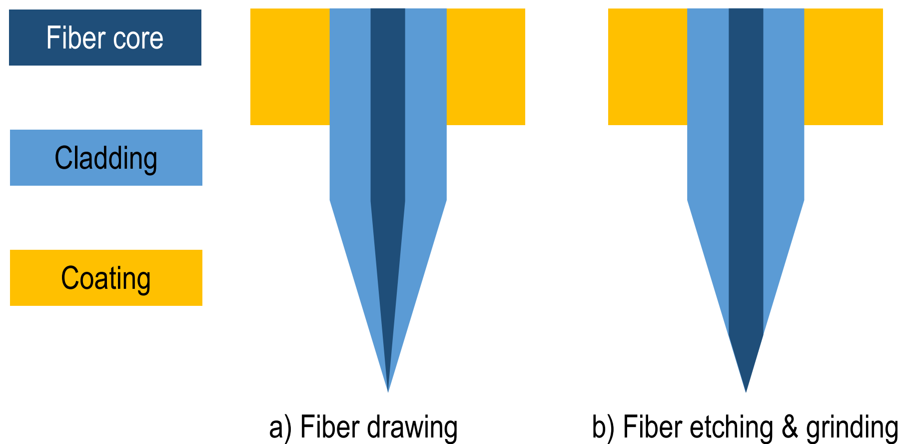

Figure 3.2 Comparison of Optical Fiber Tapering Methods

Abrasion based fiber sharpening techniques are capable of creating curved lenses and multifaceted end face profiles, but require specialized computer driven nano-stages and high speed air spindles and bearings [54], [55]. Abrasion and etching methods remove cladding and core material indiscriminately and tapers are controlled be abrasion angle and etch rate. Unlike heat-driven drawing processes, abrading and etching have no effect on the core and cladding size within the fiber, and fibers tapered smaller than the core diameter the fibers experience significant energy loss from the exposed core.

Fiber etching techniques use concentrated hydrofluoric acid (HF) to etch the silica fiber into a sharpened tip. HF is an extremely corrosive contact poison, and must be handled safely. Using an immiscible organic solvent as a protection layer above the HF provides a level of

operator safety and provides several notable advantages. The protection layer maintains the etchant concentration by preventing evaporation, prohibits vapor etching of the fiber, and results in self-terminating fiber tapers [56]. The meniscus height formed between the etchant and organic solvent is directly related to the contact diameter of the fiber and the organic solvent used in the protection layer. As the fiber diameter decreases over time due to etching, the meniscus height decreases, creating the linear taper profile illustrated in **Error! Reference ource not found.** [57]. This process self-terminates when the fiber tip diameter reaches zero.

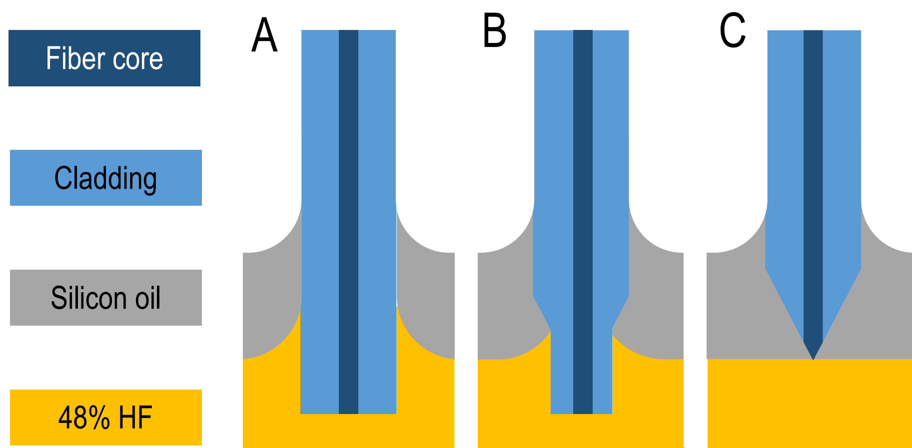

Figure 3.3 Self Terminating Fiber Etching Technique. (A) Stripped fiber is inserted into HF solution with silicon oil protection layer. (B) Silicon oil protects the freshly etched fiber surface. (C) The etching process terminates as the fiber diameter below the protection layer approaches zero.

Prior to the tapering process, the acrylate coating of the optical fibers was removed. Existing techniques for removing the polymer coating involve dipping fibers for 20 seconds in sulfuric acid at 190°C [58], [59]. A safer and simpler method of submersion in commercially available paint stripper (Zip-Strip, Star Bronze Company, Alliance, OH) and wiping with an IPA-soaked KimWipe was used to remove the polymer coating and produced identical results. Stripped fibers were rinsed with acetone, DI water, and dried with filtered dry nitrogen.

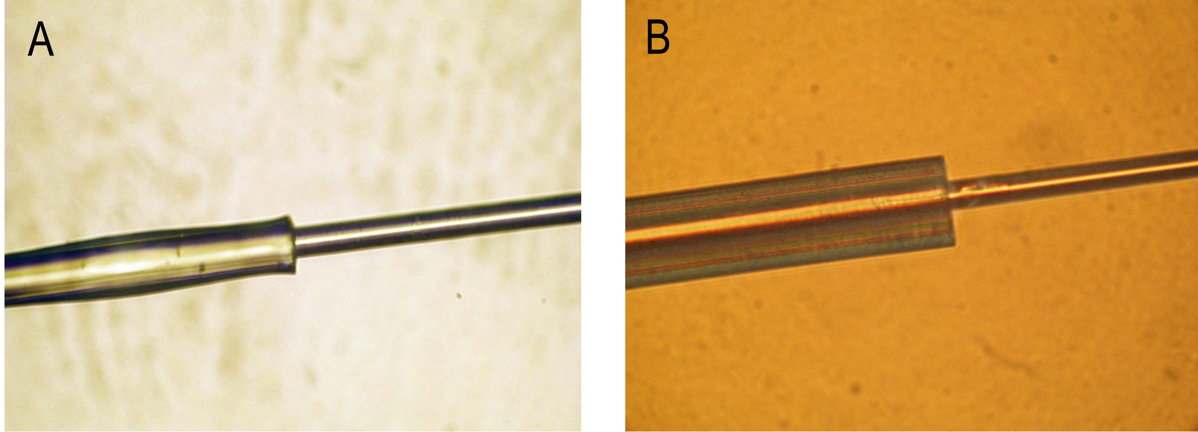

Figure 3.4 Comparison of Stripped Optical Fibers. (A) Fiber coating stripped using heated sulfuric acid and (B) Zip-Strip paint stripper. Sulfuric acid submersion causes local degradation of the coating, while the paint stripper compound leaves the coating intact.

The protection layer chemical etching method is capable of producing cone angles ranging from 8° to 41° depending on the organic solvent used and temperature of the etchant bath [57]. In the fabrication of narrowed fibers for incorporation into implantable MEAs, cone angles smaller than 8° may be desirable to minimize the overall dimensions of the implanted fiber. Because the material removal rate during etching is based on the surface area of the substrate exposed to the etchant solution, altering the insertion depth of the fiber in the etchant solution allows for greater variation of taper dimensions than standard protection layer etching. Analogous to increasing the insertion depth of the fiber, the etchant level can be raised by means of displacement as a chemically inert rod is lowered into the etchant solution. Highly controlled cone angles of 0.85° have been routinely achieved with this modification to the protection layer method.

The stripped fiber ends were mechanically cleaved to ~1 cm and secured onto a vertical fiber holding fixture. The etchant bath was prepared by dispensing 100 mL of undiluted 48% hydrofluoric acid (HF) and 20 mL of silicon oil into a polypropylene container [56]. The silicon oil and HF are immiscible liquids and a protection layer of silicon oil assembles/forms on the surface of the bath. The fiber holding fixture was mounted above the etchant container and the

exposed fiber end was carefully lowered into the etchant bath until it extended below the silicon oil layer. A PMMA displacement rod was mounted to a micropositioner and lowered in the HF with a constant feed rate to create an elongated taper angle. After etching to the desired profile, fibers were thoroughly rinsed in DI water and dried using filtered dry nitrogen.

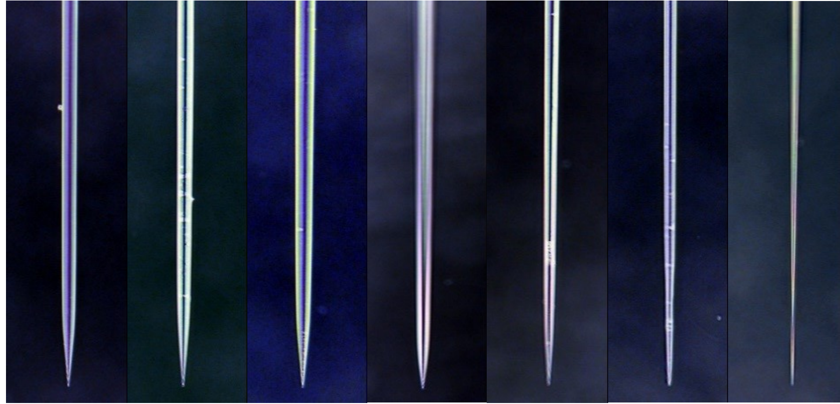

Figure 3.5 Tapered Fibers Produced with Various Cone Angles. Different cone angles are achieved through control of the HF solution displacement rate

3.3 Selective Metallization on Tapered Fibers

Etching is capable of producing highly tunable taper shapes at the expense of removing the cladding surrounding the core. The tuned refractive index mismatch between the core and cladding is responsible for maintaining the total internal reflectance of light within the core. With the cladding layer removed, the reflection and refraction of light at the boundary of the core can be described by the Fresnel equations. When shallow taper angles are produced (<5°), excessive leakage of light from refraction occurs, as the length of taper is directly related to the area of uncladded core. Coating the uncladded core of the fiber with highly reflective metal retains light in the tapered core. Physical vapor and chemical deposition methods can be used to coat fiber tapers but methods for preventing occlusion of the tip must also be used, as these are nonspecific deposition processes. In this project phase, physical vapor deposition (PVD) and

chemical deposition were investigated for producing a metallized coating that prevents optical losses along the taper while still allowing forward emission of light at the fiber tip.

The first technique employed for depositing a metal film on the tapered fibers was EBPVD. The EBPVD process bombards a metal anode with an electron beam, causing atoms of the target to vaporize and coat all line-of-sight surfaces within the chamber [60]. Because of the line-of-sight deposition involved with EBPVD, the cylindrical fibers were oriented parallel to the anode and coated once, then rotated 180° and coated again to create a uniform coating over the entire taper. Fibers were coated with to 1000 Å thickness with titanium alone, titanium coated with gold, titanium coated with copper, and chromium coated with gold. In these fibers, the deposited metal films coated the fiber, but also obscured the tip, preventing efficient light transmission.

Chemical deposition of metal on the tapered fibers was also explored. The non-conductivity of the silica fibers limits metal film deposition processes and the smooth surfaces of the fiber impede metal adhesion. A commonly employed method of chemically depositing metal on non-conductive substrates is electroless plating, a non-galvanic process that is compatible with a variety of metals and substrates. Electroless plating is an auto-catalytic reaction that involves sensitization of the substrate by a reducing agent followed by rapid metal deposition in a plating bath containing dissolved metal ions [61]. Compared to EBPVD, electroless plating offers a high efficiency and rapid plating of metal, as the deposition occurs only on the sensitized substrate. Electroless nickel, copper, silver, and gold deposition processes are well established and sensitization and plating solutions are commonly available from commercial vendors.

An electroless silvering solution was initially used to test the feasibility of applying a metal coating to the fiber tips (HE-300 silvering solution, Peacock Laboratories, Philadelphia PA). The silvering solution consists of sensitizer, silver, activator, and reducer solutions. Large

diameter (~1 mm diameter) glass fibers were etched, cleaned with DI water, and submerged in the stannous chloride sensitizer solution for 20 seconds. The sensitized fibers were dipped into a container of DI water and immediately dipped into a well containing a mixture of the silver, activator, and reducer solutions at 23°C for 3 minutes. The fiber tips were uniformly coated with silver, verifying the possibility of applying metal to tapered optical fibers using electroless chemical deposition.

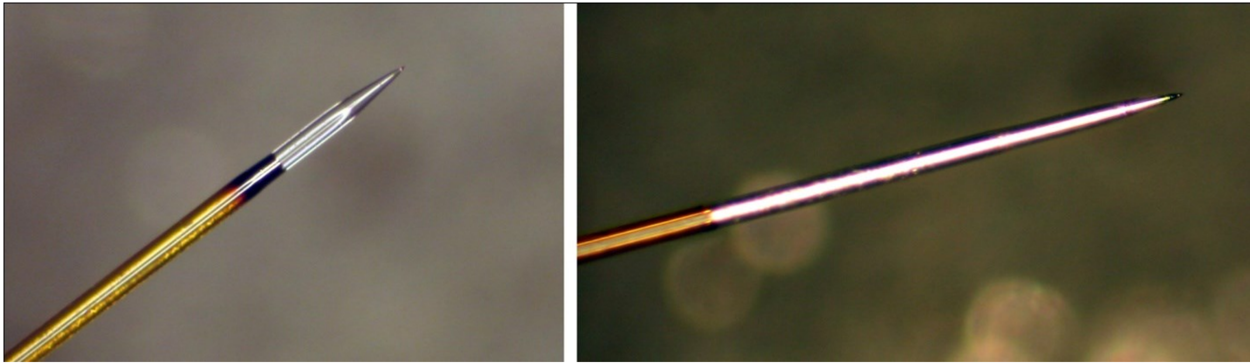

Figure 3.6 Tapered Fibers Coated with Silvering Solution.

An adherent copper deposition system for thru-hole plating was used to confirm the ability to coat optical fibers with metal. Copper electroless plating is often used in the electronics industry to deposit electrical traces and plate the interior of via holes in circuit boards. The electroless copper plating system used (PC Electroless Copper, Transene Company, Inc., Danvers MA) consisted of a surface sensitizing solution, an activator solution, and an electroless copper plating bath. Stripped and cleaved 100 μm diameter optical fibers were cleaned of oils with acetone, dipped into a 10% sulfuric acid solution to remove insoluble salts, rinsed in DI water, and then submerged in a 33% HCL solution as stated in the plating directions. The fibers were moved directly into the surface sensitizing solution at 23°C for 2 minutes, rinsed in DI water, allowed to stand in the activator solution at 23°C for 2 minutes, and rinsed again in DI water. The electroless copper plating bath was heated to 40°C under mild agitation and fibers

were successfully plated at the rate of 0.2 mil/hour. All processed surfaces of the fibers were robustly plated with copper, leading to the conclusion that tapered fibers could also be plated in this manner.

3.4 Fiber Truncation

The chemical and physical vapor deposition processes used to metallize the tapered fibers indiscriminately coat the entirety of the fibers, preventing efficient optical transmission through the fiber tip. A method of creating an aperture at the tip of the metallized fiber was developed to allow for forward optical transmission while preserving the metal coating. Truncating the tip to create an orthogonal face on the end of the fiber increases efficient light transmission by exposing the fiber core, enlarging the aperture, and preserving the metal coating.

Methods of truncating very finely tapered optical fibers by machining and polishing were explored. Workpiece fixturing is a necessary component of any machining process and requires special consideration when delicate and brittle structures are involved. The truncation method explored in this project involved embedding the fiber in a sacrificial material, machining the bulk of this material along with the encapsulated fiber, then dissolving the sacrificial material, allowing the truncated fiber to be safely removed.

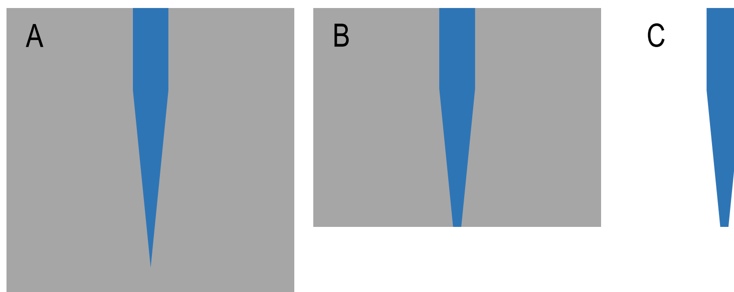

Figure 3.7 Fiber Truncation Process. (A) Fibers are embedded in a sacrificial material. (B) The bulk material and encapsulated fiber are simultaneously machined. (C) The sacrificial material is dissolved, leaving a truncated fiber.

PMMA was chosen as a sacrificial material because it is rigid and easily machinable, can be welded to itself using hot embossing methods, and is readily dissolved in solvents. Hot

embossing of PMMA is achieved by placing a small amount of solvent on the surfaces of PMMA, then applying pressure and heat to weld the pieces together. This approach allowed tapered fibers to be successfully encapsulated in PMMA slides by aligning the fiber between the slides and hot embossing to effectively seal the PMMA around the fiber. Because the hot embossing process requires the transfer of heat to the interstitial space between the pieces, thin slides of 1/16" PMMA were used to facilitate heat conduction and reduce the pressure needed to fuse the slides around the fiber. Two drops of methanol were applied on top of a 1" square PMMA slide, a fiber was laid in the pool of methanol, a second PMMA slide was placed on top of the fiber, and the entire assembly was placed in a hot embossing press at 82°C. The embossing press was closed with gentle pressure for 60 seconds and the fused PMMA-fiber assembly was removed.

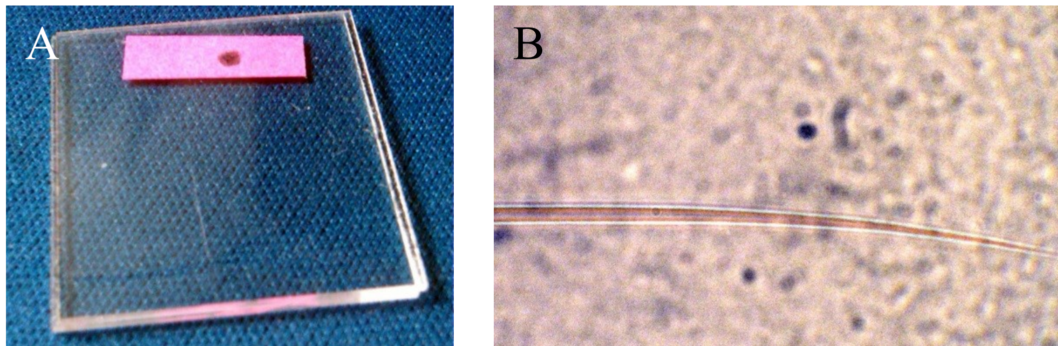

Figure 3.8 Tapered Optical Fiber Encapsulated in Sacrificial PMMA Carrier

It was discovered that fibers placed in careful alignment with the edge of the PMMA slide prior to embossing would tend to shift out of place or curl to a significant degree. This is believed to be due to a combination of the methanol flowing towards the edges of the slides as they are compressed and torsional forces between the slides as the embossing press is tightened. This misalignment can be seen in **Error! Reference source not found.**, and fibers would ccasionally become misaligned by more than 90° from their initial position.

After embossing the PMMA slides, an electric table saw was used to create a fresh working edge. The fiber positions were inspected and the new working edge was cut perpendicular to the fiber tip. This allowed for minor adjustment on workpieces in which the fiber tip became misaligned by a small amount.

A lapping process was selected for material removal because it is highly controllable and compatible with glass grinding and polishing given the correct sanding compound is chosen. Machining with steel or carbide tools was believed to lead to chipping and shattering of the brittle fiber during machining and was not investigated. Varying levels of abrasive grit were used to gradually remove the bulk material and polish the truncated fiber tip. Initially, rough grit sandpaper (600 grit) was used to remove PMMA ahead of the fiber tip. The lapping process was monitored by visual inspection of the fiber through the PMMA slides. Intermittently during lapping, the PMMA assembly would be removed and inspected via inverted microscope so the truncation of the fiber could be closely monitored. Once the fiber tip was exposed, 1500 grit, 5 μm, and 1 μm sandpaper was used to grind the working surface, and standard copy paper was used to perform the final polish of the fiber tip once the truncation step was complete.

After sufficient truncation and polishing of the fiber was achieved, the fiber was released from between the two PMMA slides. Initially the PMMA slides were dissolved by soaking in pure acetone at 23°C for 60 minutes, but it was later discovered that mechanical separation of the PMMA slides yielded the same result with a low risk of damaging the fiber.

In order to handle longer lengths of fiber and facilitate removal of the truncated fiber, the PMMA slides were increased in size and machined along the edges to aid in the mechanical separation of the slides.

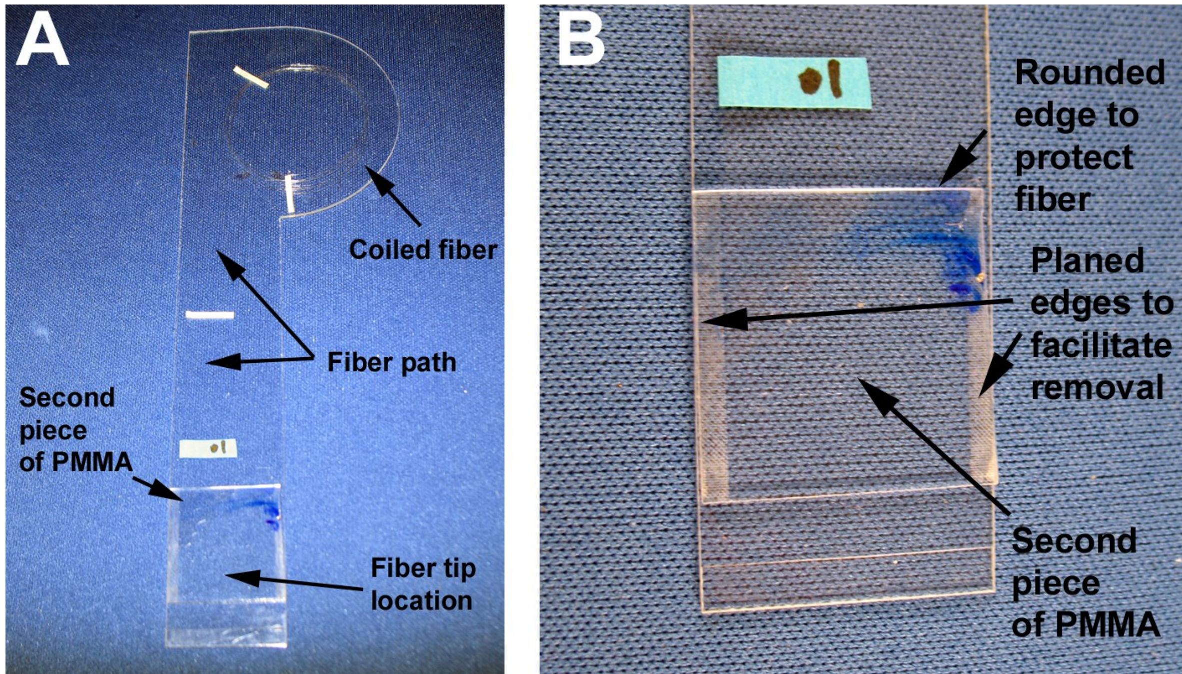

Figure 3.9 Optical Fiber Carrier. (A) 1 meter total length optical fiber mounted on carrier. Tapered fiber end is encapsulated and ready for polishing. (B) Detail of fiber tip holder.

The thin size of the PMMA slides was advantageous during hot embossing and facilitated visual inspection of fibers during truncation, but hindered the bulk machining process because the workpiece was so narrow that keeping the fiber perpendicular to the grinding surface was difficult. Therefore, a custom jig was created to clamp the PMMA-fiber assembly, keeping it perpendicular to the grinding medium and allowing small adjustments to be made to the machining angle.

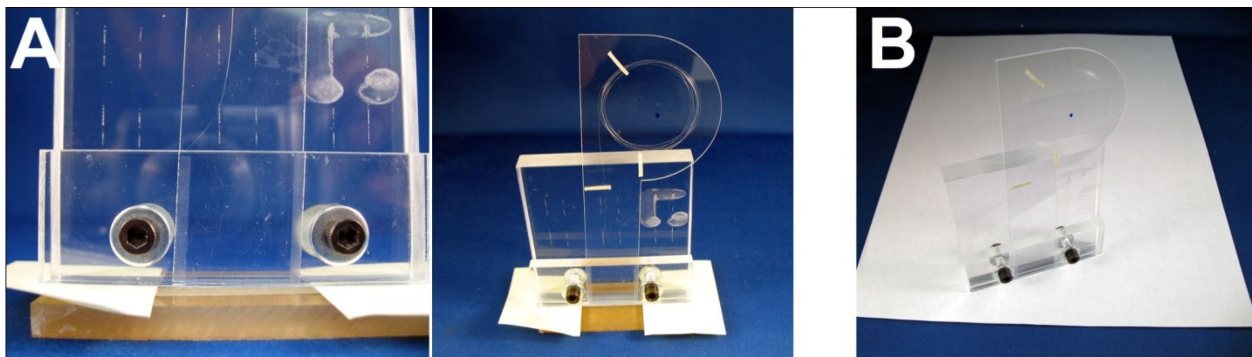

Figure 3.10 Alignment Jig for Fiber Truncation. (A) The fiber holder is clamped in the jig and spacers are used to advance the fiber end from the bottom surface of the jig. The jig assists in maintaining orthagonality of the fiber during lapping. (B) Copy paper was used to polish the fiber end prior to release.

The following images show multiple fibers that have been truncated according to the process described. While the optical properties of these truncated fibers have not been quantitatively evaluated, it is recognized that the flatness, orthagonality, and surface quality of the truncated face are not optimal. Polishing medium, grit size, and cutting speed represent key parameters in surface finish quality and control. Further experimentation with the polishing method would likely yield better surface finish and optical transmission capabilities. It is unknown if the hot embossing process or the release method causes damage to the core of the fiber. The materials and methods used in fixturing the fibers could be modified if necessary. A thermal release agent or rigid fixture for holding multiple fibers is envisioned for future development of this process. Automation and multiplexing in etching, polishing, and inspection are believed to yield more and better quality fibers.

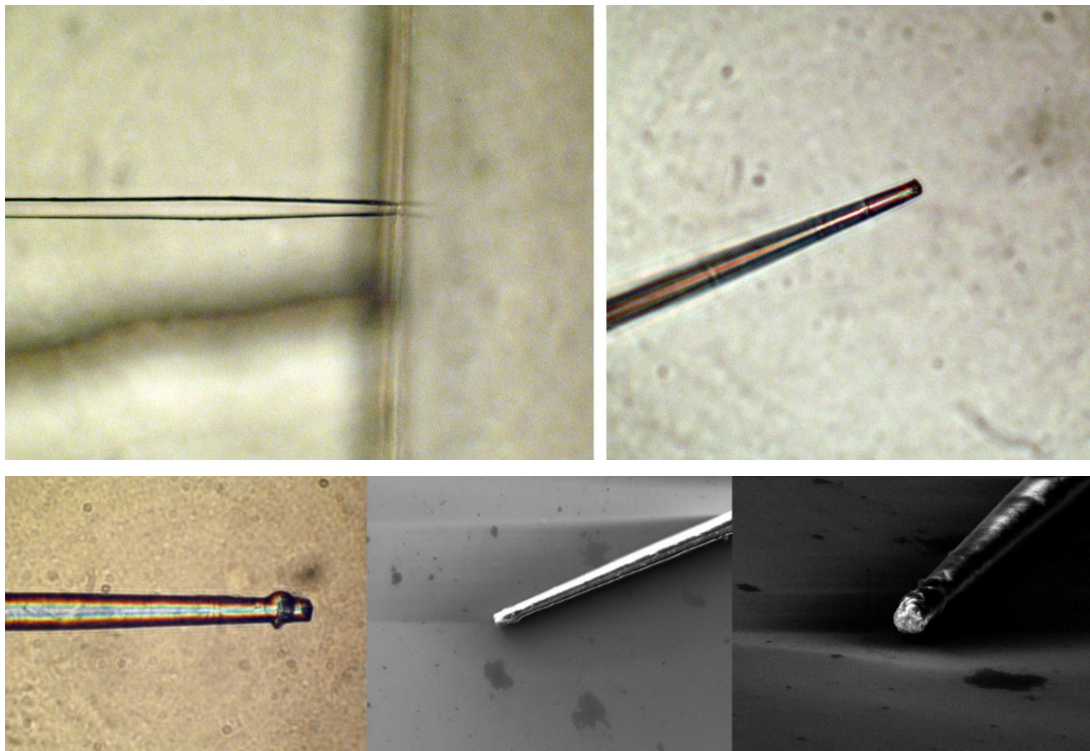

Figure 3.11 Tapered and Truncated 25 μm Optical Fibers.

A method for truncating tapered fibers with a high level of control was developed but not optimized. The process is compatible with the metallization processes described in section 3.4 and capable of producing apertures that allow the escape of light from the truncated face at the end of tapered and metallized fibers.

3.5 Optical Focusing and Scattering

Methods for focusing and scattering light emitted from the fiber tips were investigated. It may be necessary to provide optical stimulation across a very small volume of tissue to achieve high levels of selectivity in an optoelectrode. Alternatively, a more diffuse light pattern may be desired to prevent localized heating caused by high energy density on a very small fiber tip. The incorporation of a shaped lens or scattering element on the tip of a fiber core was believed to achieve these output modes. Methods of forming and attaching lenses and scattering elements to optical fibers by photolithographic processes, glass fusing, and micromolding were investigated.

Optical fibers are ideally suited for photolithographically defined lenses and apertures, as the core of the fiber can be used to transmit light for photoresist exposure. A positive photoresist becomes soluble to a developer when exposed to light while the unexposed region remains insoluble while a negative photoresist becomes insoluble to developer when exposed to light. Thus it can be imagined that a positive photoresist may be useful for creating apertures at the core of a fiber, while a negative photoresist can be used to create a plug over the core of the fiber. The ability to create these structures on the end of optical fibers was explored.

The photoresists used during this investigation were selected based on their adhesion to silica, viscosity during processing, and optical properties. Shipley 1827 (MICROPOSIT SC 1827 Positive Photoresist) provides excellent adhesion to a variety of substrates and is routinely used to produce 2.7 μm coatings. As positive photoresist, Shipley 1827 would be removed along

the core, so optical properties were not considered. 1002F-10 (EPON Resin 1002F) is a negative photoresist capable of producing 10 μm thick coatings, has strong adhesion to silica, exhibits low autofluorescence, displays unique reflow properties when exposed to post processing heating, and can be premixed with optical scattering additives.

100 cm long 25 μm diameter optical fiber segments were stripped of their coating at the tip, cleaved, and cleaned and dried as previously described. Fibers ends were coated with positive and negative photoresist by hand dipping into pools of Shipley 1827 and 1002F-10 until a dimple was seen on the surface of the photoresists. Because of surface tension, the photoresist would form drops behind the fiber tip (**Error! Reference source not found.** (a)) if excessive hotoresist was applied. Photoresist coating of the fiber tips was verified by visual inspection and for the purpose of this investigation a thick or non-uniform coating on the fibers was permitted. The fibers were soft baked at 75°C for 10 minutes then 95°C for 20 minutes to solidify the uncured liquid photoresists.

To couple the fiber to a light source for exposure of the photoresist, the uncoated fiber ends were inserted into a bare fiber adaptor (Newport F-AS-ST Bare Fiber Adaptor) and connected to a UV light source (Analytical Instrument Systems DT-1000CE) with a measured light intensity of 1.5 mW/cm^2. The optimal exposure time for photoresist coated fibers was experimentally determined to be 5 minutes. This relatively long exposure time is likely due to the small core diameter in these fibers and losses encountered in the light coupling step, and could be optimized with high higher efficiency fiber coupling methods.

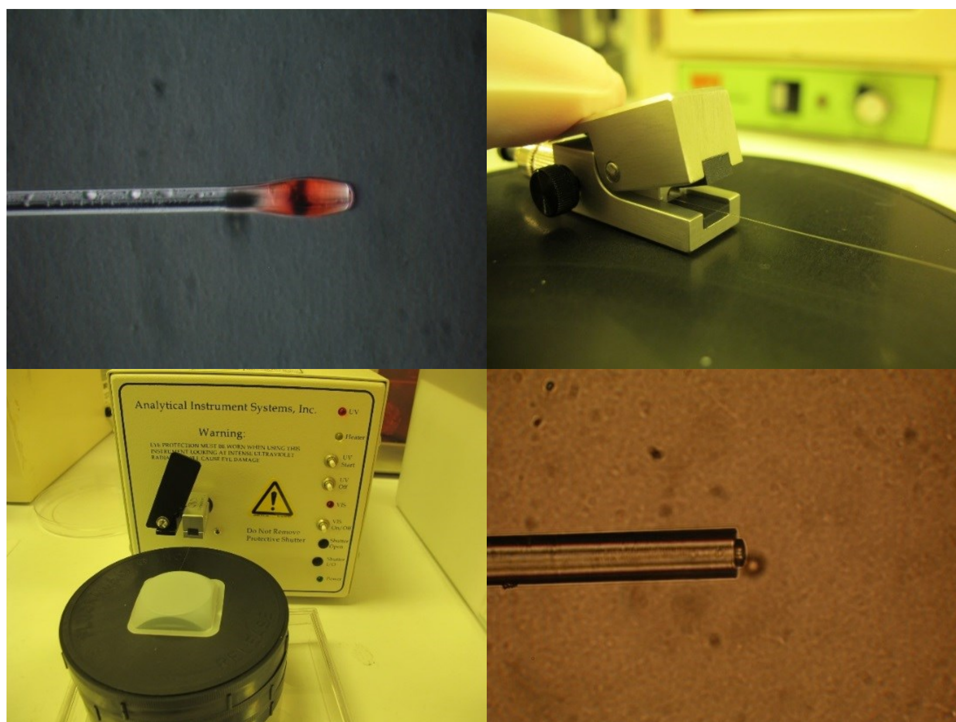

Figure 3.12 Lithographically Formed Microlenses on 25 μm Diameter Optical Fibers. (a) Cleaved optical fiber dip coated with negative photoresist. (b) Opposite fiber end inserted into light coupling fiber holder. (c) Through-fiber exposure of photoresist on cleaved fiber end. (d) Resulting structure with well-defined boundaries.

The Shipley 1827 and 1002F-10 coated fibers were transferred to a carrier plate and post-exposure baked at 65°C for 5 minutes and 95°C for 10 minutes, then developed with MF-319 (Microposit MF-319 Developer) and SU-8 developer, respectively, for 15 seconds. After a final bake at 120°C for 30 minutes, the fibers were removed and inspected.

Photoresist was noticeably absent on the tips of fibers coated in positive photoresist. In tapered fibers subjected to this process, entire regions of the tip were visible, and it was believed that these regions were areas with etched cladding. Optical transmission was qualitatively observed from these apertures, but the positive photoresist used was not opaque to light. It can be reasoned that this method of fiber coating may be useful as a means of applying an opaque coating to the fiber that prevents light transmission along a taper. Methods to produce a more uniform coating and further optimize exposure would likely yield higher levels of control in aperture creation.

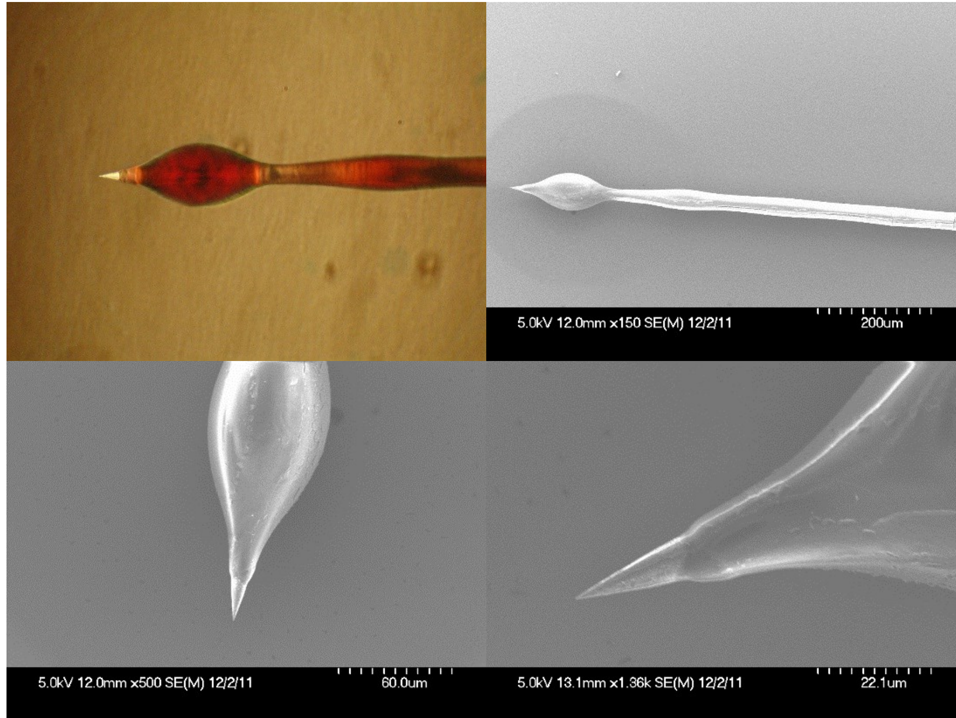

Figure 3.13 Through-fiber Exposure of Positive Photoresist on Tapered Fiber. While the photoresist was clearly exposed along the fiber core, the photoresist edge was poorly defined. This is believed to be due to non-uniformity of photoresist coating on the fiber.

Fibers processed with negative photoresist produced well-defined curved 1002F structures over the core of the fibers. The height of these structures was defined by the thickness of the photoresist on the fiber end while the circular shape was defined by the core size in the fiber. The slight curvature on the surface of the structure is due to the surface tension of the liquid photoresist during application. 1002F can be reflowed somewhat by heating and this property could be utilized to create lenses on the ends of fibers with higher radii of curvature than observed here. Optical scattering additives such as barium sulfate or titanium dioxide can be homogeneously added to the liquid photoresist to produce a composite structure. Interestingly, this process creates identical structures on broken fibers, since the emission of light is still confined to the core of the fiber. This illustrates the flexibility of this process, as lens structures may be produced on non-cleaved fibers that are more easily produced.

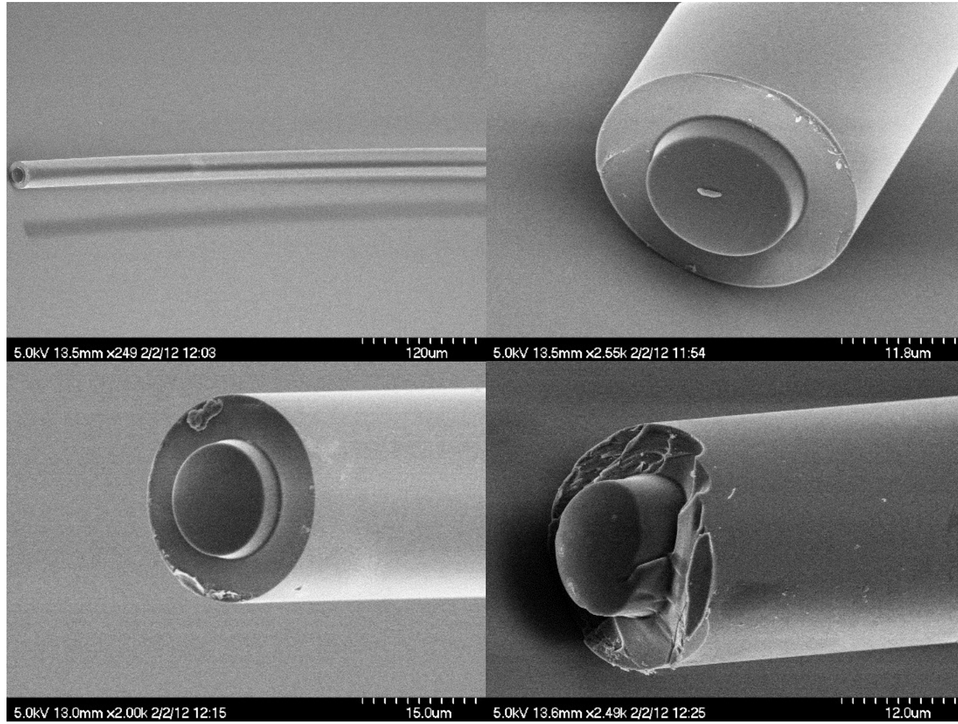

Figure 3.14 Cleaved and Broken 25 μm Optical Fibers with Negative Photoresist Structures.

Alternative methods for creating lenses were explored. Fusing 30 μm borosilicate glass microspheres to the ends of 25 μm diameter fibers by heating with a nichrome resistance wire heating element was demonstrated. A significant advantage of fusing borosilicate glass to the silica fiber is the strong adhesion created by the covalent network bonding that occurs at the interface. Heating temperatures and timing were approximate, as the fusion of the elements was completed under visual inspection alone. Light propagation through the lens is demonstrated in **Error! Reference source not found.**, showing the wide angle scattering of light in the spherical lass lens. While these tests were completed with non-cleaved fibers, it is believed that fibers with cleaved faces would exhibit better self-centering of the lens due to surface tension. Commercially available glass microspheres are highly variable in size and spheres with sub-micrometer tolerances would be ideal for attachment to fibers.

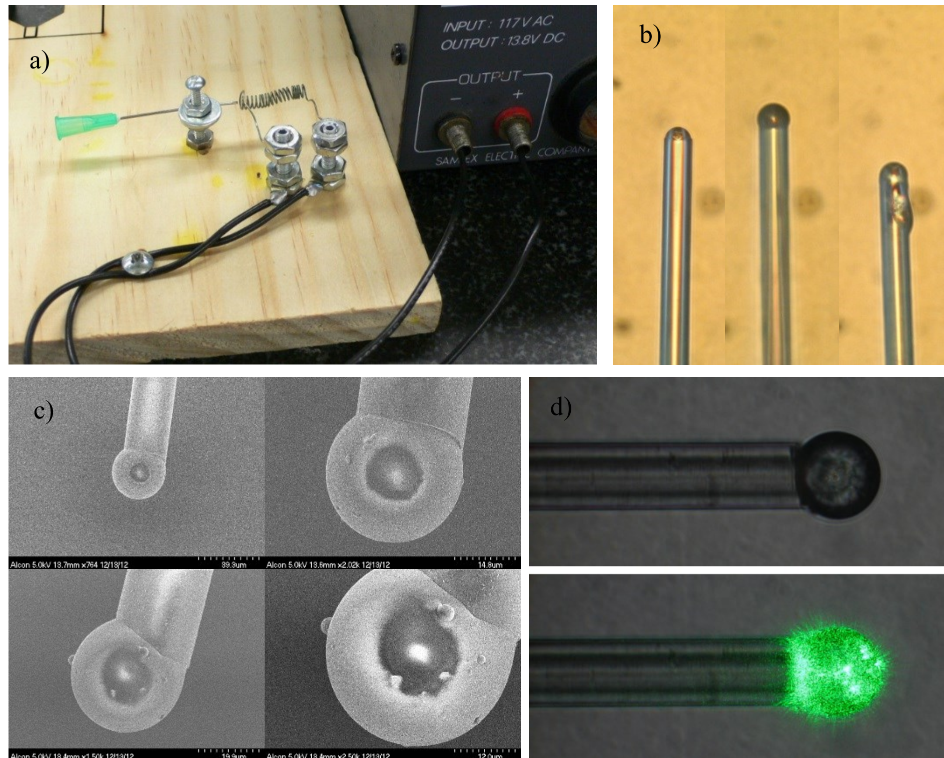

Figure 3.15 Optical Fibers with Fused Glass Microlenses. (a) Early prototype of micro furnace for fusing glass spheres on fiber ends. (b) Various lens shapes can be produced. (c) SEM of fused glass microlens on 25 µm optical fiber. (d) Light transmission through the attached microlens.

Finally, molding and casting methods for producing pre-formed microlenses were investigated. Casting is used as a process to accurately replicate macro and micro structures of an item by forming a substrate material against a shaped mold. The quality of the casting is highly dependent upon the properties of the casting liquid and mold material, as the casting liquid should penetrate all features of the mold but allow release of the part once the liquid has cured.

A silicon mold was created using dry plasma etching techniques. A square mesh with 20 x 20 µm openings and 10 µm wide streets was patterned onto a 4 inch silicon wafer with Shipley 1827 photoresist. The silicon wafer was subjected to deep reactive-ion etching (DRIE) and stripped of photoresist to achieve 20 x 20 µm square openings with 10 µm depth. This negative silicon master mold was cast against a thermoplastic polymer (Evonik Trogamid CX) to create a

positive master mold. Pressure was applied between the silicon and heated polymer during a hot embossing process to create a partial replication of the silicon mold. The resulting hemispherical lens shape created on the polymer surface (**Error! Reference source not found.**) is caused by ncomplete embossing of the thermoplastic polymer and can be manipulated by modifying the temperature and pressure applied to the polymer during embossing.

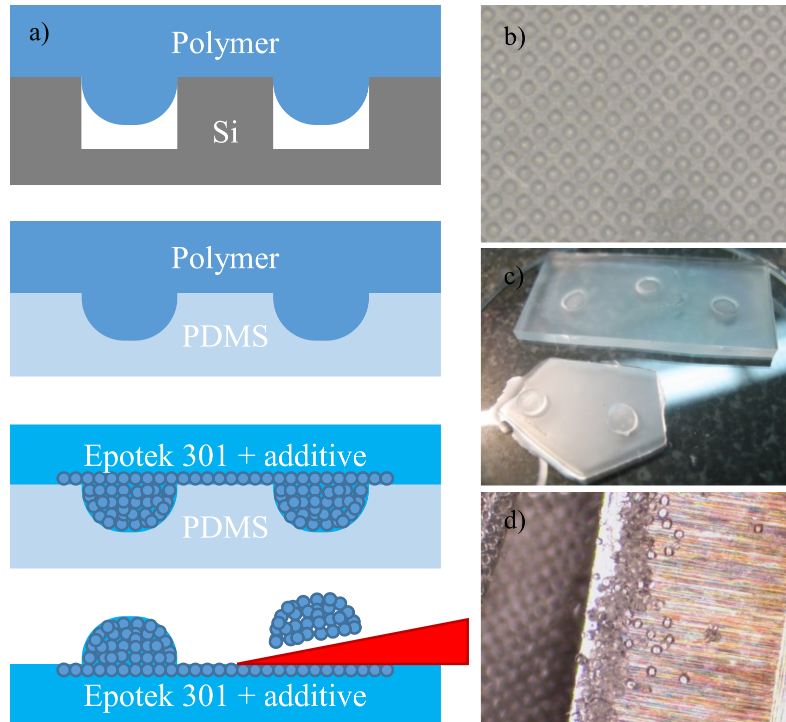

Figure 3.16 Diagram of Microlens Pre-form Fabrication Process. (a) Polymer is partially embossed against a negative silicon mold to create a positive mold. PDMS is cast against the positive mold to create a soft negative mold. Various casting compounds and optical scattering additives can be cast against the PDMS mold to form microlenses. (b,c,d) Optical micrographs of microlenses.

A negative mold was created with polydimethylsiloxane (PDMS), a two-part hydrophobic silicone polymer, cast against the positive polymer master mold. PDMS was mixed in a 10:1 ratio and poured over the polymer master mold before degassing and curing at 80°C for 8 hours [62]. The low surface free energy of PDMS allowed the negative mold to be easily separated from the polymer master mold. The low viscosity optical epoxy adhesive Epotek 301 was selected as a microlens substrate material due to its optical clarity and ease of incorporating

optical additives to increase light scattering within the microlens. For the purpose of creating a light scattering lens, 5 μm diameter borosilicate glass spheres were scattered over the PDMS negative mold and Epotek 301 was mixed and poured over the glass spheres. Once cured, the Epotek 301 was removed from the PDMS negative mold and cut from the substrate with a sharp blade. The resulting structures can be seen in **Error! Reference source not found.**. The glass icrospheres were well-distributed within the microlenses. It was noted that the cut surfaces of the formed microlenses was not ideal, but these lenses could be separated from the bulk casting by embedding in a sacrificial layer and machined from the backside to create flat mounting surfaces. The flexibility to incorporate many diverse additives is a major advantage of this micromolding process, which is capable of producing monolithic and composite lenses in bulk.

This process can be adapted to create pre-forms for use with sintering, a method that involves binding glass or metal particles into a particular shape, then heating to pyrolyze the binder and fuse the particles into the shape of the pre-form. Sintered glass microlenses with micro or nanoscale voids are capable of both diffusing and scattering light.

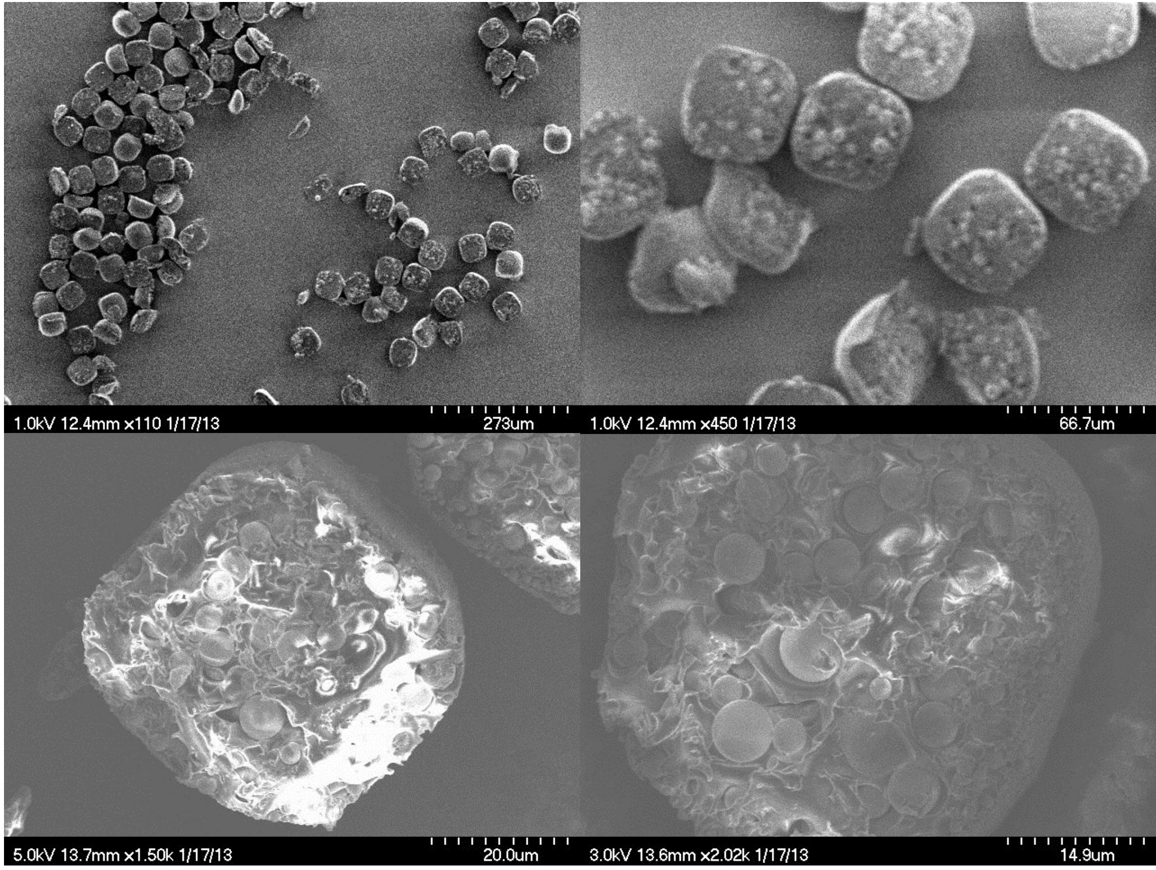

Figure 3.17 Composite Microlenses Formed with EPO-TEK 301 and 5 μm Borosilicate Glass Spheres.

CHAPTER 4: FLEXIBLE STIMULATING MICROELECTRODE ARRAY

4.1 Introduction

A major concern in the application of chronically implantable electrodes is the mechanical stresses and strains that are caused by the pulsatile movement of the tissue surrounding the electrode. A portion of the electrode is commonly tethered to bone and the electrode is routed into the soft tissue in the immediate vicinity. While the bone provides a rigid support for holding the electrode in place, the soft tissue may experience large movement relative to that bone, resulting in large movements between the electrode and the tissue. The rigidity of the electrode shank, the wire bundle, and the interconnects have been implicated as the causes of this mechanical stress. Silicon based MEAs are inherently rigid due to the material properties of silicon and monolithic nature of these devices and microwire electrode stiffness is related to the diameter and number of wires. An electrode that is flexible enough to travel with the natural motion of the tissue is thought to be able to overcome this major drawback. Presented here is a means of producing a slim profile flexible electrode from evaporated metal on a polymer substrate using existing silicon fabrication techniques. A reliable and high-yield three mask process is described.

A modified shank MEA was created using photolithographic methods to define a MEA that is thin, flexible, and made from biocompatible materials. The thin-film MEA comprised lithographically patterned conductive gold traces encapsulated between biocompatible insulation layers with circular openings along the shank revealing stimulation sites. The flexible MEA is 25 μm thick across its entirety and features a 250 μm wide tapering shank with eight stimulation sites having 200 μm pitch in either 200 μm^2 or 400 μm^2 configurations. The integrated cabling

is 2 cm long and provides gold connection points for attachment to the same interfacing PCB used in the hybrid shank MEA.

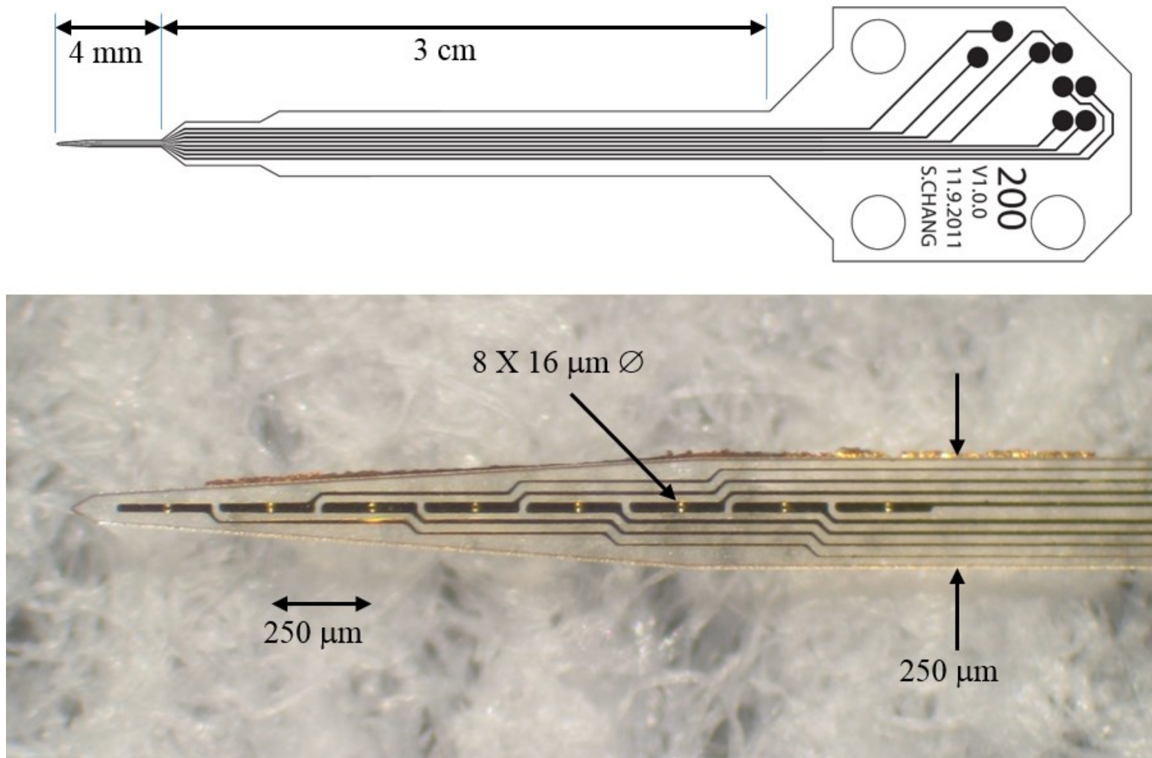

Figure 4.1 Flexible Polymer MEA Overview.

4.2 Microfabrication of Flexible Microelectrode Arrays

The flexible MEA was designed with a minimal number of layers order to provide a reliable and high-yield process. The part quality and yield of a given lithographic process is inversely related to the number of masks used and layers involved. Photomasks are manually aligned on the substrate by the user under high magnification and the tolerances involved in aligning masks stack on each subsequent layer. This tolerance stacking results in potentially large and catastrophic offsets between the first and last layer in multi-mask processes.

The thin film MEA described in this section is fabricated using a three mask process. An initial layer of biocompatible polymer is photopatterned on the substrate to define the overall shape of the device. A second mask patterns the conductive traces on a layer of deposited metal.

A final layer of 1002F encapsulates the metal traces and defines the exposed electrode sites. The electrodes were released from the substrate through an etching step.

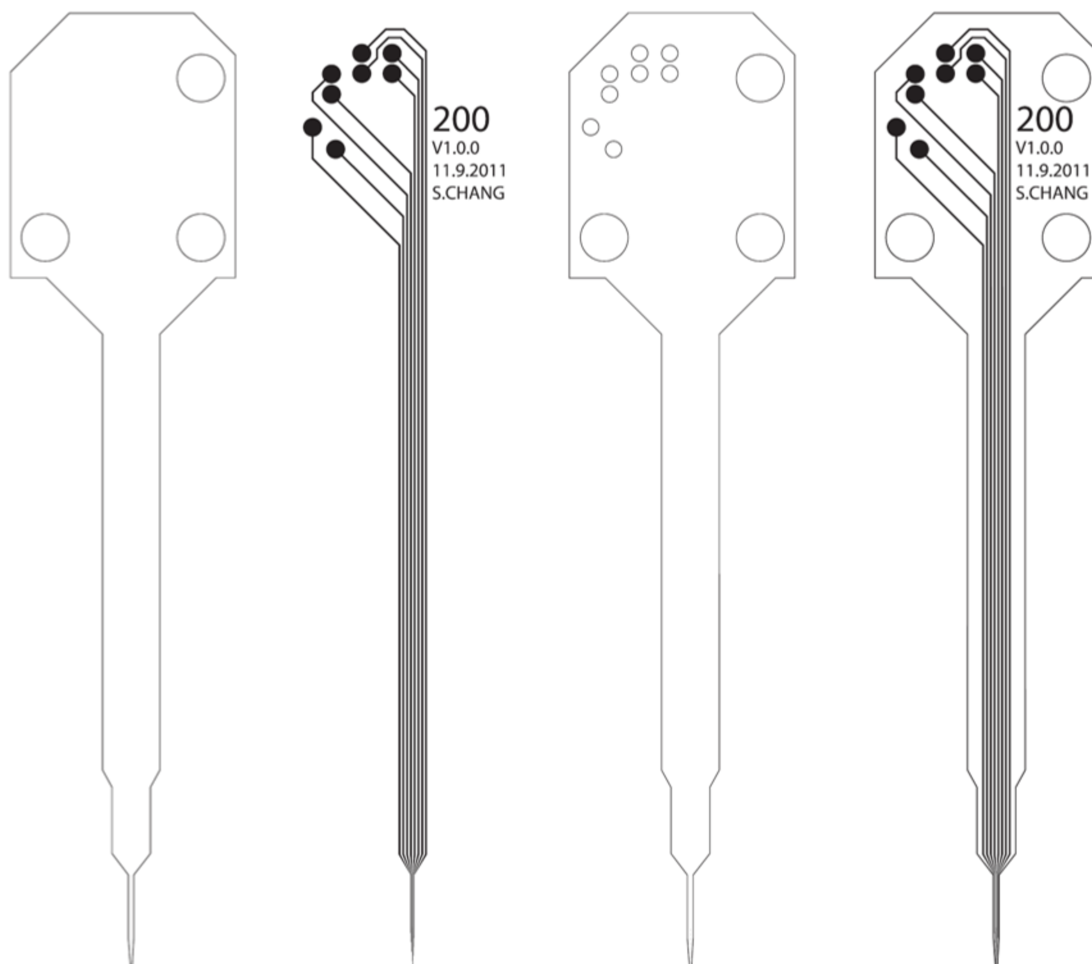

Figure 4.2 Photomasks Used in Polymer MEA Fabrication.

Photolithography masks were designed and digitally rendered with Adobe Illustrator software and printed into emulsion film photo masks. The lithography masks were transferred from the flexible emulsion masks to iron oxide coated soda lime glass photoplates (Ferroxoplate, Towne Technologies, Inc., Somerville, NJ) using the following procedure. The photoplates were pre-coated with 5000 Å thickness Shipley 1827 positive photoresist and baked in a convection oven at 95°C for 30 minutes. The photoplate was loaded into a Karl Suss MA56 Mask Aligner

with the emulsion side of the film mask immediately in contact with the photoresist layer of the hard mask. The aligned masks were exposed to ultraviolet light for 7 seconds under a 275 watt mercury vapor lamp filtered for 365 nm wavelength, removed from the aligner, and lightly agitated in Shipley developer (MF-319) for 30 seconds before rinsing in DI water and drying under filtered dry nitrogen. The exposed iron oxide layer on the glass mask was etched in an HCl-ferrous chloride solution for 5 minutes before stripping the remaining photoresist. The masks were rinsed in DI water, blown dry, and heated to 120°C for 45 minutes as per manufacturers guidelines to increase film hardness and chemical resistance. The mask transfer process was repeated for each of the masks, resulting in three photoplates corresponding to the three layers of the device.

A 6" silicon wafer was cleaned by rinsing with acetone and IPA then dried with nitrogen and dehydrated for 30 minutes at 120°C. 1002F-10 photoresist was spin coated onto the prepared silicon wafer at 2000 rpm for 30 seconds to achieve a 12 μm uniform thickness. The spin coating parameters for the particular batch of photoresist were empirically tested and measured by profilometer. The liquid photoresist was soft baked for 10 minutes at 65°C then 95°C to dry and harden the 1002F-10.

The first photomask was used to pattern the basement 1002F-10 layer. The 1002F-10 coated substrate and first mask were loaded into a Karl Suss MA56 photoaligner and exposed to UV light for 10 seconds. The workpiece was removed and subjected to a post-exposure bake for 5 minutes at 65°C and 10 minutes at 95°C. The unexposed photoresist was developed for ~30 seconds in SU-8 developer and the substrate temperature was ramped to 120°C over 10 minutes in convection oven, held for 30 minutes, and ramped down to 35°C for 15 minutes.

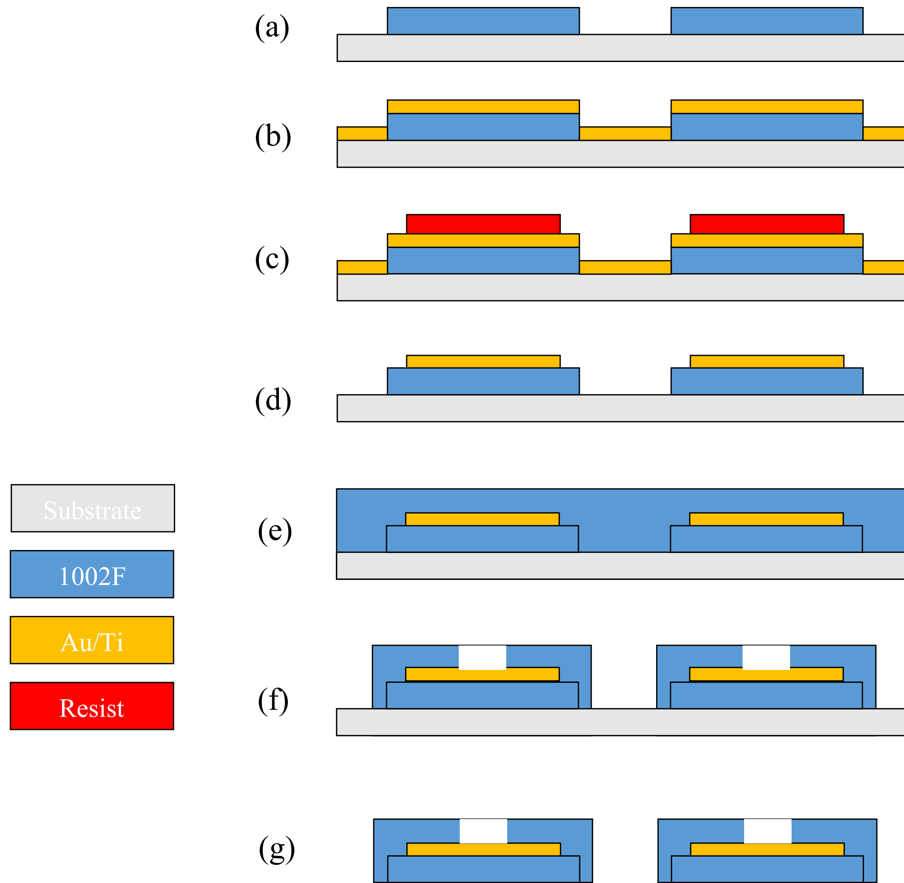

Figure 4.3 Fabrication Process for Polymer MEA. (a) Basement polymer layer is patterned. (b-d) Metal is deposited and patterned by etching. (e-f) Encapsulating polymer layer is patterned. (g) Electrode release from substrate.

The workpieces were placed into an E-beam evaporator (Temescal CV-14) and deposited with gold to a thickness of 2000Å. Shipley 1827 photoresist was spin coated uniformly above the gold layer to 2.7 µm thickness. The second mask containing the metal traces was aligned over the workpieces using precision alignment marks located on the periphery of the mask. The Shipley photoresist was exposed for 23 seconds and developed for 25 seconds. The workpieces were submerged in potassium iodide (1:4:40 $I_2/KI/H_2O$) gold etchant solution for 80 seconds and lightly agitated to removed exposed gold. Because of the low thickness of the evaporated gold, there was very little under etching observed in the devices. The remaining Shipley photoresist was stripped with acetone, and the workpieces were rinsed with IPA and dried with nitrogen.

The third polymer layer was designed with an overlap of the first polymer layer to seal the metal traces between polymer layers. The overlapping region doubles the surface area in contact between the first and third layers and serves to prevent delamination of the 1002F-10 layers. The final 1002F-10 layer was spin coated on the workpiece above the gold traces to a thickness of 23 μm using the same parameters already described. The final 1002F-10 layer was patterned and developed as described above. The devices were baked at 120°C for 45 minutes to reflow the 1002F-10 and create a high strength bond by fusing the polymer layers together. Scanning electron micrographs of several devices are presented in **Error! Reference source not ound.**. Circular apertures along the shank correspond to the electrode sites.

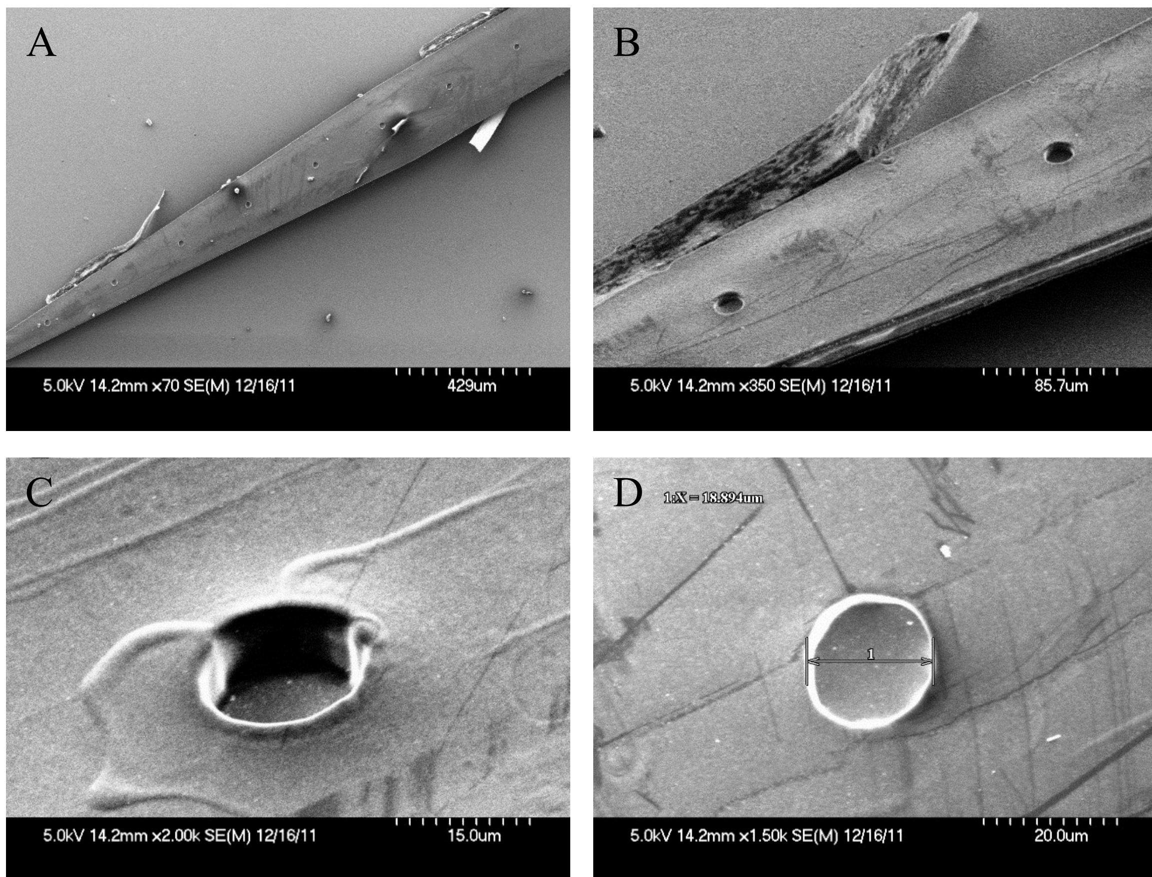

Figure 4.4 SEM of Polymer MEAs.

During the manufacture of these electrodes, several substrate modifications were needed to overcome difficulties in releasing the final devices. Electrodes were initially fabricated directly on silicon wafers that provide a highly planar and rigid substrate for creating high quality devices but the aggressive acid etching process required for device release led to device destruction. Copper foil substrates facilitated release of the final electrode via non-destructive etching, but the poor surface quality of the raw copper foil transfers to the backside of the devices, leaving a rough surface. Copper coated liquid crystal polymer (LCP) with higher quality surface finish than copper foil was also used, but a longer under-etching process was required to release the devices from the LCP substrate.

The final step of releasing the electrodes from the substrates involved multiple strategies based on the substrate material. The first strategy involved dissolving the entire silicon substrate, and a hydrofluoric-nitric-acetic acid (HNA) isotropic backside etch process was used. A mixture of 160 ml acetic acid, 60 ml of nitric acid, and 20 ml of hydrofluoric acid was measured into a polypropylene container and the substrate wafer was placed into the aggressive etchant solution. After 20 minutes the electrode tips began lifting off, but the large surface area and strong adhesion of 1002F-10 to silicon prevented rapid release and the etch was continued for three hours. At this point, the 1002F-10 was chemically altered and rendered useless for further processing. The devices subjected to prolonged HNA etch can be seen in **Error! Reference ource not found.** (b).

A secondary strategy involved the use of a copper foil substrate that would be dissolved in a backside etching process. Because metal foils lack the rigidity to maintain flatness during vacuum fixturing for spin coating and mask alignment, the 125 μm thick copper foil was cut to shape and adhered to a silicon wafer using a thermal release tape (REVALPHA, Semiconductor

Equipment Corp., Moorpark CA). The initial processing and fabrication steps were identical to the silicon substrate devices. Once complete, the copper foil was peeled from the silicon wafer and dissolved in a ferric chloride etchant solution to release the devices. Unlike the HNA release, the mild ferric chloride copper etchant did not cause any noticeable chemical change to the 1002F-10 substrate, but the surface texture of the copper foil (seen in **Error! Reference ource not found.** (c)) was transferred to the device.

The final release strategy employed an under-etch process on a copper coated LCP substrate. An advantage of the LCP substrate over the bare copper foil is its relative thickness; it was rigid enough to be used in place of a silicon wafer during the fabrication process. The electrodes were lithographically fabricated on the copper surface. The LCP substrate was submerged in ferric chloride and held at 45°C under light agitation while the copper layer was under-etched from between the LCP and devices. Because the copper etchant was exposed to a small surface area relative to the total copper area under the devices, the release took place over several hours. Once electrodes were at least 90% separated from the substrate, they were transferred to a clear ammonium persulfate etchant solution so that the final release could be carefully monitored. Released electrodes floated to the surface of the etchant and were rinsed with DI water and dried. The devices built on LCP substrate presented a higher quality surface than those fabricated on copper foil, with a tradeoff of extended release time and exposure to the etchant solution.

Electrical connection to the interfacing PCB was made with conductive epoxy (8331 Silver conductive epoxy adhesive, M.G. Chemicals, Surrey, B. C.). Conductive epoxy was dispensed onto each of the gold pads on the electrode, and the PCB was aligned over the pads and lowered into place.

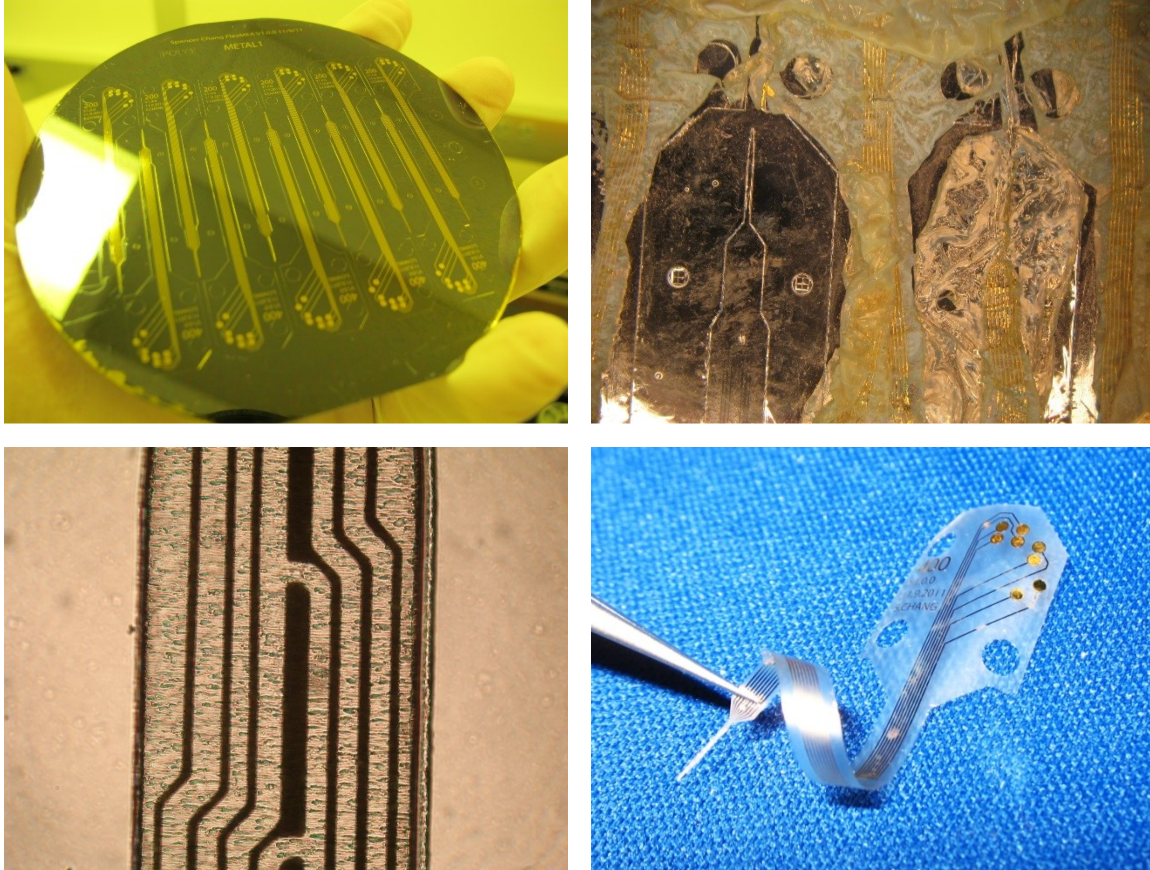

Figure 4.5 Polymer MEA. (a) Devices prior to release. (b) HNA release methods were unsuccessful as they caused significant degradation of the electrode substrate material. (c) Optical micrograph of released electrode from copper substrate. The surface finish of the copper foil substrate transferred to the polymer. (d) Flexible polymer MEA.

4.3 Future Directions

Experiments to create high quality coatings with favorable electrical properties and strong adhesion should be conducted as a next step. The flexible electrode presented here did not include any deposited surface treatments that enhance charge transfer from the electrode to tissue. Coating the electrode sites with electrically favorable neural stimulation materials should be investigated. Sputtered, evaporated, or electrochemically deposited iridium oxide are well characterized processes and could be easily integrated into the fabrication process presented here. Poly(ethylenedioxythiophene) (PEDOT), an electrically conductive polymer coating that can be doped with biomolecules to enhance biocompatibility, exhibits favorable charge-injection capacity for stimulating electrodes [5]. PEDOT can be electrochemically deposited onto the

electrode using the interfacing PCB to access each stimulation channel. Carbon nanotubes (CNTs) are an emerging material that offer a high ESA to GSA ratio and can be modified to enhance biocompatibility. An appealing trait of both PEDOT and CNTs is the ability to chemically modify the coatings to enhance the biocompatibility and functionality of the electrodes.

The surgical implantation of the electrode should be considered in future design revisions. While the flexibility of the electrode is crucial in reducing mechanical damage to the tissue over time, it may hinder insertion of the electrode into tissue. It would be desirable to devise a means for inserting the flexible electrode into the tissue of interest without sacrificing the flexibility of the electrode as an implant. One scheme that can be imagined involves a releasable stiffener that, upon insertion into the tissue of interest, can be separated from the electrode and removed from the tissue without additional force being exerted on the electrode. This on-demand release could be accomplished by a mechanical, electrical, chemical, thermal, or biodegradation process that would rapidly release the stiffener from the electrode. A critical requirement of this release method would be to maintain biocompatibility by preventing the discharge of any harmful by-products into the tissue.

The physical and electrical properties of the devices need to be characterized and evaluated before these devices can become useful research tools. The relationship between polymer thickness and stiffness of the final device would provide insight on the ability of the device to move with its surrounding tissue, as well as its ability to penetrate the tissue of interest without buckling. Chemical analysis of the device consistent with ISO 10993 standards may reveal whether any residual toxic compounds remain in the final device or if the biocompatibility of the device is compromised by any materials used. The electrical properties of the electrode

should be measured via electrochemical impedance spectroscopy (EIS) and cyclic voltammetry to assess the extent and quality of the electroactive coating on the electrode sites. Testing protocols should be fully established in this device.

The focus of this investigation was not the mass production of implantation-ready stimulating devices, but rather to show the feasibility of creating flexible polymer electrodes from biocompatible materials using lithographic processes. The fabrication processes described represent a starting point for future investigations involving alternate biocompatible materials, designs, and fabrication processes. Once an ideal fabrication process and materials are identified, the individual processes and recipes should be optimized for device quality and yield.

CHAPTER 5: CONCLUSION

The main goal of the current study was to explore the capabilities of hybrid microfabrication by creating stimulation and recording microelectrode arrays and optical components for optoelectrodes. A hybrid microfabrication approach was used to fabricate multi-channel shank MEAs using tool-based micromachining, microwire assembly, molding, and electrodeposition. The flexibility of this approach was illustrated by creating precisely tapered optical fibers and composite fiber mounted microlenses for micro-optoelectrode applications using wet etching, micromolding, embossing, lapping, and lithography. MEMS and traditional photolithographic techniques were used to create a thin and flexible polymer-based MEA. Taken together, these results suggest that hybrid microfabrication techniques are advantageous in several respects. First, by integrating microfabrication techniques that do not rely on specific chemical and material interactions are compatible with a wide range of dissimilar materials, and a large amount of design flexibility is afforded in the types of substrates and component materials that can be used. Second, hybrid microfabrication techniques allow engineers to fabricate micrometer sized devices and components in complex three-dimensional geometries that would otherwise be difficult or impossible to create without highly complex and prohibitively expensive apparatuses. Finally, hybrid microfabrication techniques afford improved integration of handling, fabrication, assembly, and packaging in microscale devices.

The goal of the work presented here is to provide a baseline for future studies and investigations into hybrid microfabrication techniques for the creation of microelectrodes and microelectrode components. While many techniques were shown to have great potential, optimization of process throughput and device performance was not a primary objective and as such no individual process was explored in great depth. Further work needs to be done to

optimize these processes as well as establish other hybrid microfabrication techniques involving emerging materials, technologies, and microfabrication processes. While this study provided special emphasis on microelectrode array fabrication, it is clear that the hybrid approach to microfabrication will enable the creation of countless novel microdevices.

BIBLIOGRAPHY

[1] Y. Li and D. J. Mogul, "Electrical control of epileptic seizures," *J. Clin. Neurophysiol.*, vol. 24, no. 2, pp. 197–204, 2007.

[2] J. C. Middlebrooks and R. L. Snyder, "Selective Electrical Stimulation of the Auditory Nerve Activates a Pathway Specialized for High Temporal Acuity," *J. Neurosci.*, vol. 30, no. 5, pp. 1937–1946, Feb. 2010.

[3] J. S. Perlmutter and J. W. Mink, "Deep brain stimulation," *Annu Rev Neurosci*, vol. 29, pp. 229–257, 2006.

[4] R. A. Normann, "Technology Insight: future neuroprosthetic therapies for disorders of the nervous system," *Nat. Clin. Pract. Neurol.*, vol. 3, no. 8, pp. 444–452, Aug. 2007.

[5] S. F. Cogan, "Neural Stimulation and Recording Electrodes," *Annu. Rev. Biomed. Eng.*, vol. 10, no. 1, pp. 275–309, Aug. 2008.

[6] R. V. Shannon and S. R. Otto, "Psychophysical measures from electrical stimulation of the human cochlear nucleus," *Hear. Res.*, vol. 47, no. 1–2, pp. 159–168, Aug. 1990.

[7] D. R. Merrill, M. Bikson, and J. G. R. Jefferys, "Electrical stimulation of excitable tissue: design of efficacious and safe protocols," *J. Neurosci. Methods*, vol. 141, no. 2, pp. 171–198, Feb. 2005.

[8] S. B. Brummer and M. J. Turner, "Electrochemical considerations for safe electrical stimulation of the nervous system with platinum electrodes," *Biomed. Eng. IEEE Trans. On*, no. 1, pp. 59–63, 1977.

[9] K. C. Cheung, "Implantable microscale neural interfaces," *Biomed. Microdevices*, vol. 9, no. 6, pp. 923–938, Oct. 2007.

[10] D. A. Robinson, "The electrical properties of metal microelectrodes," *Proc. IEEE*, vol. 56, no. 6, pp. 1065–1071, 1968.

[11] K. C. Cheung, K. Djupsund, Y. Dan, and L. P. Lee, "Implantable multichannel electrode array based on soi technology," *J. Microelectromechanical Syst.*, vol. 12, no. 2, pp. 179–184, Apr. 2003.

[12] W. L. C. Rutten, "Selective Electrical Interfaces with the Nervous System," *Annu. Rev. Biomed. Eng.*, vol. 4, no. 1, pp. 407–452, Aug. 2002.

[13] M. A. Nicolelis, D. Dimitrov, J. M. Carmena, R. Crist, G. Lehew, J. D. Kralik, and S. P. Wise, "Chronic, multisite, multielectrode recordings in macaque monkeys," *Proc. Natl. Acad. Sci.*, vol. 100, no. 19, pp. 11041–11046, 2003.

[14] D. T. Kewley, M. D. Hills, D. A. Borkholder, I. E. Opris, N. I. Maluf, C. W. Storment, J. M. Bower, and G. T. . Kovacs, "Plasma-etched neural probes," *Sens. Actuators Phys.*, vol. 58, no. 1, pp. 27–35, Jan. 1997.

[15] T. H. Yoon, E. J. Hwang, D. Y. Shin, S. I. Park, S. J. Oh, S. C. Jung, H. C. Shin, and S. J. Kim, "A micromachined silicon depth probe for multichannel neural recording," *Biomed. Eng. IEEE Trans. On*, vol. 47, no. 8, pp. 1082–1087, 2000.

[16] P. Norlin, M. Kindlundh, A. Mouroux, K. Yoshida, and U. G. Hofmann, "A 32-site neural recording probe fabricated by DRIE of SOI substrates," *J. Micromechanics Microengineering*, vol. 12, no. 4, p. 414, 2002.

[17] K. D. Wise, A. M. Sodagar, Ying Yao, M. N. Gulari, G. E. Perlin, and K. Najafi, "Microelectrodes, Microelectronics, and Implantable Neural Microsystems," *Proc. IEEE*, vol. 96, no. 7, pp. 1184–1202, Jul. 2008.

[18] D. R. Kipke, R. J. Vetter, J. C. Williams, and J. F. Hetke, “Silicon-substrate intracortical microelectrode arrays for long-term recording of neuronal spike activity in cerebral cortex,” *IEEE Trans. Neural Syst. Rehabil. Eng.*, vol. 11, no. 2, pp. 151–155, Jun. 2003.
[19] M. D. Gingerich, J. F. Hetke, and D. J. Anderson, “A 256-site 3D CMOS microelectrode array for multipoint stimulation and recording in the central nervous system,” presented at the Int. Conf. Solid-State Sensors and Actuators, Munich, Germany, 2001.
[20] Y. Lu, Y. Zhang, J. Lu, A. Mimura, S. Matsumoto, and T. Itoh, “Three-dimensional photolithography technology for a fiber substrate using a microfabricated exposure module,” *J. Micromechanics Microengineering*, vol. 20, no. 12, p. 125013, Dec. 2010.
[21] K. E. Petersen, “Silicon as a mechanical material,” *Proc. IEEE*, vol. 70, no. 5, pp. 420–457, 1982.
[22] P. J. Rousche, D. S. Pellinen, D. P. Pivin Jr, J. C. Williams, R. J. Vetter, and others, “Flexible polyimide-based intracortical electrode arrays with bioactive capability,” *Biomed. Eng. IEEE Trans. On*, vol. 48, no. 3, pp. 361–371, 2001.
[23] X. Liu, R. E. DeVor, S. G. Kapoor, and K. F. Ehmann, “The Mechanics of Machining at the Microscale: Assessment of the Current State of the Science,” *J. Manuf. Sci. Eng.*, vol. 126, no. 4, p. 666, 2004.
[24] D. . Stephenson, D. Veselovac, S. Manley, and J. Corbett, “Ultra-precision grinding of hard steels,” *Precis. Eng.*, vol. 25, no. 4, pp. 336–345, Oct. 2001.
[25] V. Piotter, “Micro injection moulding of components for microsystems,” presented at the Proc. of the 1st Euspen topical conference on fabrication and metrology in nanotechnology, Copenhagen, Denmark, 2000, pp. 182–189.
[26] E. M. Kjaer, “Micro injection moulding,” presented at the Proc. of the 1st Euspen topical conference on fabrication and metrology in nanotechnology, Copenhagen, Denmark, 2000, pp. 259–267.
[27] F. Z. Fang, K. Liu, T. R. Kurfess, and G. C. Lim, “Tool-based micro machining and applications in MEMS,” in *MEMS/NEMS*, Springer, 2006, pp. 678–740.
[28] N. Taniguchi, “Current Status in, and Future Trends of, Ultraprecision Machining and Ultrafine Materials Processing,” *CIRP Ann. - Manuf. Technol.*, vol. 32, no. 2, pp. 573–582, Jan. 1983.
[29] L. Alting, F. Kimura, H. N. Hansen, and G. Bissacco, “Micro Engineering,” *CIRP Ann. - Manuf. Technol.*, vol. 52, no. 2, pp. 635–657, Jan. 2003.
[30] D. Dornfeld, S. Min, and Y. Takeuchi, “Recent Advances in Mechanical Micromachining,” *CIRP Ann. - Manuf. Technol.*, vol. 55, no. 2, pp. 745–768, Jan. 2006.
[31] K. Yamanaka, “Anodically Electrodeposited Iridium Oxide Films (AEIROF) from Alkaline Solutions for Electrochromic Display Devices,” *Jpn. J. Appl. Phys.*, vol. 28, no. Part 1, No. 4, pp. 632–637, Apr. 1989.
[32] C. D. Breach and F. W. Wulff, “A brief review of selected aspects of the materials science of ball bonding,” *Microelectron. Reliab.*, vol. 50, no. 1, pp. 1–20, Jan. 2010.
[33] R. D. Meyer, S. F. Cogan, T. H. Nguyen, and R. D. Rauh, “Electrodeposited iridium oxide for neural stimulation and recording electrodes,” *Neural Syst. Rehabil. Eng. IEEE Trans. On*, vol. 9, no. 1, pp. 2–11, 2001.
[34] P. T. Kissinger and W. R. Heineman, “Cyclic voltammetry,” *J. Chem. Educ.*, vol. 60, no. 9, p. 702, 1983.
[35] P. J. Rousche and R. A. Normann, “Chronic recording capability of the Utah Intracortical Electrode Array in cat sensory cortex,” *J. Neurosci. Methods*, vol. 82, no. 1, pp. 1–15, 1998.

[36] S. Trasatti and O. A. Petrii, “Real surface area measurements in electrochemistry,” *J. Electroanal. Chem.*, vol. 327, no. 1, pp. 353–376, 1992.
[37] J. D. E. McIntyre, “Oxidation State Changes and Structure of Electrochromic Iridium Oxide Films,” *J. Electrochem. Soc.*, vol. 127, no. 6, p. 1264, 1980.
[38] R. S. Nicholson, “Theory and Application of Cyclic Voltammetry for Measurement of Electrode Reaction Kinetics.,” *Anal. Chem.*, vol. 37, no. 11, pp. 1351–1355, 1965.
[39] J. D. Weiland and D. J. Anderson, “Chronic neural stimulation with thin-film, iridium oxide electrodes,” *Biomed. Eng. IEEE Trans. On*, vol. 47, no. 7, pp. 911–918, 2000.
[40] D. B. McCreery, W. F. Agnew, T. G. Yuen, and L. Bullara, “Charge density and charge per phase as cofactors in neural injury induced by electrical stimulation,” *Biomed. Eng. IEEE Trans. On*, vol. 37, no. 10, pp. 996–1001, 1990.
[41] D. B. McCreery, T. G. H. Yuen, W. F. Agnew, and L. A. Bullara, “Stimulus parameters affecting tissue injury during microstimulation in the cochlear nucleus of the cat,” *Hear. Res.*, vol. 77, no. 1, pp. 105–115, 1994.
[42] E. S. Boyden, F. Zhang, E. Bamberg, G. Nagel, and K. Deisseroth, “Millisecond-timescale, genetically targeted optical control of neural activity,” *Nat. Neurosci.*, vol. 8, no. 9, pp. 1263–1268, 2005.
[43] F. Zhang, L.-P. Wang, M. Brauner, J. F. Liewald, K. Kay, N. Watzke, P. G. Wood, E. Bamberg, G. Nagel, A. Gottschalk, and K. Deisseroth, “Multimodal fast optical interrogation of neural circuitry,” *Nature*, vol. 446, no. 7136, pp. 633–639, Apr. 2007.
[44] O. Yizhar, L. E. Fenno, T. J. Davidson, M. Mogri, and K. Deisseroth, “Optogenetics in Neural Systems,” *Neuron*, vol. 71, no. 1, pp. 9–34, Jul. 2011.
[45] A. M. Packer, B. Roska, and M. Häusser, “Targeting neurons and photons for optogenetics,” *Nat. Neurosci.*, vol. 16, no. 7, pp. 805–815, Jun. 2013.
[46] G. P. Dugué, W. Akemann, and T. Knöpfel, “A comprehensive concept of optogenetics,” in *Progress in Brain Research*, vol. 196, Elsevier, 2012, pp. 1–28.
[47] V. Gradinaru, K. R. Thompson, F. Zhang, M. Mogri, K. Kay, M. B. Schneider, and K. Deisseroth, “Targeting and Readout Strategies for Fast Optical Neural Control In Vitro and In Vivo,” *J. Neurosci.*, vol. 27, no. 52, pp. 14231–14238, Dec. 2007.
[48] I. Ozden, J. Wang, Y. Lu, T. May, J. Lee, W. Goo, D. J. O’Shea, P. Kalanithi, I. Diester, M. Diagne, K. Deisseroth, K. V. Shenoy, and A. V. Nurmikko, “A coaxial optrode as multifunction write-read probe for optogenetic studies in non-human primates,” *J. Neurosci. Methods*, vol. 219, no. 1, pp. 142–154, Sep. 2013.
[49] S. Chen, W. Pei, Q. Gui, Y. Chen, S. Zhao, H. Wang, and H. Chen, “A fiber-based implantable multi-optrode array with contiguous optical and electrical sites,” *J. Neural Eng.*, vol. 10, no. 4, p. 046020, Aug. 2013.
[50] A. V. Kravitz and A. C. Kreitzer, “Optogenetic manipulation of neural circuitry in vivo,” *Curr. Opin. Neurobiol.*, vol. 21, no. 3, pp. 433–439, Jun. 2011.
[51] F. Wu, E. Stark, M. Im, I.-J. Cho, E.-S. Yoon, G. Buzsáki, K. D. Wise, and E. Yoon, “An implantable neural probe with monolithically integrated dielectric waveguide and recording electrodes for optogenetics applications,” *J. Neural Eng.*, vol. 10, no. 5, p. 056012, Oct. 2013.
[52] E. Stark, T. Koos, and G. Buzsaki, “Diode probes for spatiotemporal optical control of multiple neurons in freely moving animals,” *J. Neurophysiol.*, vol. 108, no. 1, pp. 349–363, Jul. 2012.

[53] F. Warken, E. Vetsch, D. Meschede, M. Sokolowski, and A. Rauschenbeutel, "Ultra-sensitive surface absorption spectroscopy using sub-wavelength diameter optical fibers," *Opt. Express*, vol. 15, no. 19, pp. 11952–11958, 2007.
[54] Y. A. Gharbia and J. Katupitiya, "Experimental determination of optimum parameters for nano-grinding of optical fibre end faces," *Int. J. Mach. Tools Manuf.*, vol. 44, no. 7–8, pp. 725–731, Jun. 2004.
[55] G. Milton, "Mechanical fabrication of precision microlenses on optical fiber endfaces," *Opt. Eng.*, vol. 44, no. 12, p. 123402, Dec. 2005.
[56] B. A. F. Puygranier and P. Dawson, "Chemical etching of optical fibre tips—experiment and model," *Ultramicroscopy*, vol. 85, no. 4, pp. 235–248, 2000.
[57] P. Hoffmann, B. Dutoit, and R.-P. Salathé, "Comparison of mechanically drawn and protection layer chemically etched optical fiber tips," *Ultramicroscopy*, vol. 61, no. 1–4, pp. 165–170, Dec. 1995.
[58] V. V. Rondinella and M. J. Matthewson, "Effect of chemical stripping on the strength and surface morphology of fused silica optical fiber," in *Optical Tools for Manufacturing and Advanced Automation*, 1994, pp. 52–58.
[59] J. T. Krause, "Zero stress strength reduction and transitions in static fatigue of fused silica fiber lightguides," *J. Non-Cryst. Solids*, vol. 38–39, pp. 497–502, May 1980.
[60] K. S. SreeHarsha, *Principles of physical vapor deposition of thin films*. Amsterdam; Boston; London: Elsevier, 2006.
[61] J. Sudagar, J. Lian, and W. Sha, "Electroless nickel, alloy, composite and nano coatings – A critical review," *J. Alloys Compd.*, vol. 571, pp. 183–204, Sep. 2013.
[62] R. C. Huang and L. Anand, "Non-linear mechanical behavior of the elastomer polydimethylsiloxane (PDMS) used in the manufacture of microfluidic devices," 2005.